Key Points:
- We image velocity anomalies below the North Island, New Zealand, interpreted as deeply subducted seamounts and fluid in the downgoing plate
- Independent geological and geophysical observations corroborate our seamount interpretation
- Inferred seamounts and intraslab fluid may partly explain enigmatic, along-strike plate-coupling transition at the Hikurangi margin

Correspondence to:
B. Chow,
bhchow@alaska.edu

Evidence for Deeply Subducted Lower-Plate Seamounts at the Hikurangi Subduction Margin: Implications for Seismic and Aseismic Behavior

Bryant Chow[1,2,3] ![ORCID], **Yoshihiro Kaneko**[4] ![ORCID], **and John Townend**[1] ![ORCID]

[1]School of Geography, Environment and Earth Sciences, Victoria University of Wellington, Wellington, New Zealand, [2]GNS Science, Lower Hutt, New Zealand, [3]Now at University of Alaska Fairbanks, Fairbanks, AK, USA, [4]Department of Geophysics, Kyoto University, Kyoto, Japan

Abstract Seamounts are found at many subduction zones and act as seafloor heterogeneities that affect slip behavior on megathrusts. At the Hikurangi subduction zone offshore the North Island, New Zealand, seamounts have been identified on the incoming Pacific plate and below the accretionary prism, but there is little concrete evidence for seamounts subducted beyond the present-day coastline. Using a high-resolution, adjoint tomography-derived velocity model of the North Island, we identify two high-velocity anomalies below the East Coast and an intraslab low-velocity zone up-dip of one of these anomalies. We interpret the high-velocity anomalies as previously unidentified, deeply subducted seamounts, and the low-velocity zone as fluid in the subducting slab. The seamounts are inferred to be 10–30 km wide and on the plate interface at 12–15 km depth. Resolution analysis using point spread functions confirms that these are well-resolved features. The locations of the two seamounts coincide with bathymetric features whose geometries are consistent with those predicted from analog experiments and numerical simulations of seamount subduction. The spatial characteristics of seismicity and slow slip events near the inferred seamounts agree well with previous numerical modeling predictions of the effects of seamount subduction on megathrust stress and slip. Anomalous geophysical signatures, magnetic anomalies, and swarm seismicity have also been observed previously at one or both seamount locations. We propose that permanent fracturing of the northern Hikurangi upper plate by repeated seamount subduction may be responsible for the dichotomous slow slip behavior observed geodetically, and partly responsible for along-strike variations in plate coupling on the Hikurangi subduction interface.

Plain Language Summary Seamounts are large volcanic edifices on the seafloor that eventually make their way into subduction zones. Seamounts have been identified at various stages of subduction and are thought to either promote or suppress the occurrence of large earthquakes. It is difficult to track seamounts far into a subduction zone due to the decreasing sensitivity of most geophysical measurements with depth. In this study, we identify several distinctive seismic velocity anomalies in a high-resolution 3D velocity model of the North Island, New Zealand. The model is derived using adjoint tomography, a form of seismic imaging that optimizes the match between observed and simulated seismic waveforms. We interpret the anomalies to indicate the presence of two deeply subducted seamounts and fluid in the downgoing plate. The two seamounts are inferred to be at interface depths, with horizontal dimensions of about 10–30 km. These features are well resolved and our interpretations are supported by independent evidence including seafloor bathymetry data and the presence of nearby geophysical anomalies. We associate these seamounts with variations in slip behavior observed along the Hikurangi subduction margin and propose that they have caused permanent damage to the upper plate, thereby reducing its ability to store energy and host large earthquakes.

1. Introduction

Seamounts are prominent seafloor features found globally at convergent margins, where their eventual subduction has been observed to have significant effect on upper plate morphology, and is predicted to influence megathrust slip behavior. While shallow subduction of partially buried seamounts has been inferred to play a role in tectonic erosion and deformation of the upper plate (e.g., Dominguez et al., 1998; Von Huene & Scholl, 1991), less is known about what happens as a seamount subducts further because of the limited resolution of geophysical methods commonly used to identify subducting seamounts. Previous studies have imaged buried seamounts at shallow stages of subduction (e.g., Bangs et al., 2006; Frederik et al., 2020; Marcaillou et al., 2016; Pedley
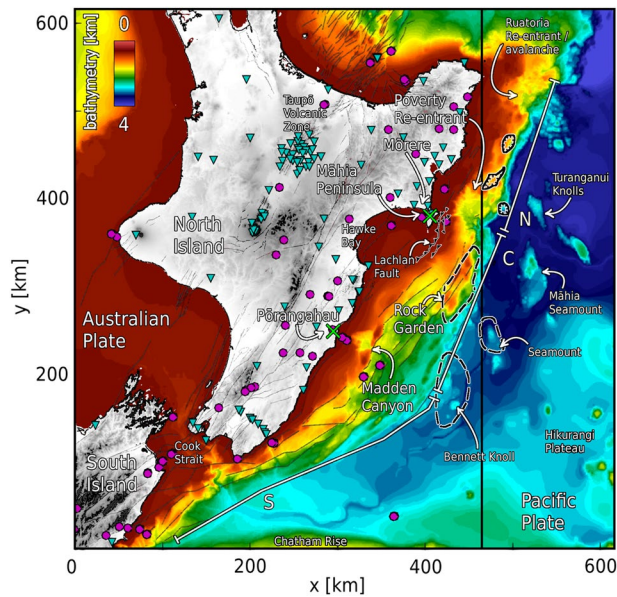
Figure 1. Tectonic setting for the Hikurangi subduction zone offshore New Zealand's North Island. High-resolution bathymetry (Mitchell et al., 2012) highlights the complicated accretionary wedge and numerous seamounts on the incoming Pacific Plate. White solid lines separate the margin into southern (S), central (C), and northern (N) segments. The solid black line at $X = 475$ km represents the eastern boundary of the model domain. Green crosses show the locations of velocity anomalies below Pōrangahau and Māhia Peninsula. Pink circles and blue inverted triangles show earthquakes and receivers used to derive the velocity model (Chow et al., 2022). Thin black lines show active faults (Litchfield et al., 2014). Seamounts identified in previous studies are shown with dashed black outlines (Barnes et al., 2010) and solid black outlines (Bell et al., 2010).

et al., 2010) and, in more limited cases, deeper into subduction zones (e.g., Kodaira et al., 2000; Martinez-Loriente et al., 2019; Singh et al., 2011).

Arguments linking subducted seamounts to large-earthquake seismogenesis are at first glance discordant, suggesting either that seamounts facilitate seismic rupture by acting as locally locked asperities on which large earthquakes can nucleate (Scholz & Small, 1997), or that they impede seismic rupture by fracturing the upper plate and rendering it incapable of storing sufficient elastic strain to produce large earthquakes (Wang & Bilek, 2011). A number of ideas have been proposed regarding the effects of seamounts on mechanical and hydrological processes in the upper plate, which may explain how subducted seamounts promote both seismic and aseismic behavior (Ruh et al., 2016; Sun et al., 2020), allow for the subduction and compaction of additional sediments to depth (Ellis et al., 2015), act as rupture barriers for large earthquakes (Yang et al., 2013), and transport inordinate amounts of fluid into subduction zones (Bell et al., 2010; Chesley et al., 2021). However, the small number of documented examples of deep seamount subduction makes it difficult to resolve the complex relationship between seamounts and slip behavior at subduction zones.

In a companion paper (Chow et al., 2022), we use adjoint tomography, an imaging technique that involves fitting short-period (>4 s) earthquake-generated seismic waveforms to corresponding synthetic waveforms, to refine a 3D velocity model of the North Island of New Zealand (Eberhart-Phillips et al., 2020). Throughout the inversion, strong velocity anomalies in the forearc region are imaged at increasing resolution. Two high-velocity anomalies are resolved as point-like structures, spanning tens of km, with peaked amplitudes at plate interface depths. We also observe a broad low-velocity zone up-dip of one of these anomalies, which reaches depths well below the predicted plate interface (Williams et al., 2013). Here, we (a) assess the robustness of those velocity anomalies in more detail, (b) interpret them as prominent tectonic features using corroborating geophysical and geological evidence, and (c) discuss the implications of such features for seismic and aseismic behavior at the Hikurangi subduction zone.

2. Hikurangi Subduction Zone

The Hikurangi subduction zone is a convergent plate boundary where the Pacific plate is subducting obliquely westward beneath the Australian plate (Figure 1). The Hikurangi margin exhibits varying differences in along-strike properties (Wallace et al., 2009), and is commonly separated into northern, central, and southern margins (Figure 1). The northern section of the margin is characterized by thin incoming sediment cover, a relatively high convergence rate (~50 km/yr), and tectonic erosion of the frontal wedge from repeated seamount subduction, resulting in a steep and narrow accretionary wedge (20–40 km). Conversely, the central and southern segments exhibit thicker incoming sediment cover (>5 km), slower (20–40 mm/yr) and increasingly oblique convergence, and a well-developed, broad, shallow-tapered accretionary wedge (30–70 km; Barnes et al., 2010; Wallace, 2020). Although relative plate motion at the Hikurangi subduction zone is oblique (and increases in obliquity southward), much of the rotational component is accommodated by right-lateral strike-slip faults in the overlying crust of the North Island (Beanland & Haines, 1998; Wallace et al., 2004, 2009). This has the effect that plate convergence rates at crustal depths are primarily margin-normal at the trench, with decreasing convergence rates from north to south (Figure 2).

The incoming seafloor at the northern Hikurangi margin (i.e., north of latitude S40°, or Y ≈ 250 km in Figure 1) is strewn with seamounts at various stages of subduction. Sediment cover here is relatively thin, and consequently numerous knolls and seamounts are identifiable in high-resolution bathymetry (Figure 1). Seamounts subducted beneath the accretionary pile have been imaged using marine seismic reflection surveys (e.g., Barker et al., 2009;
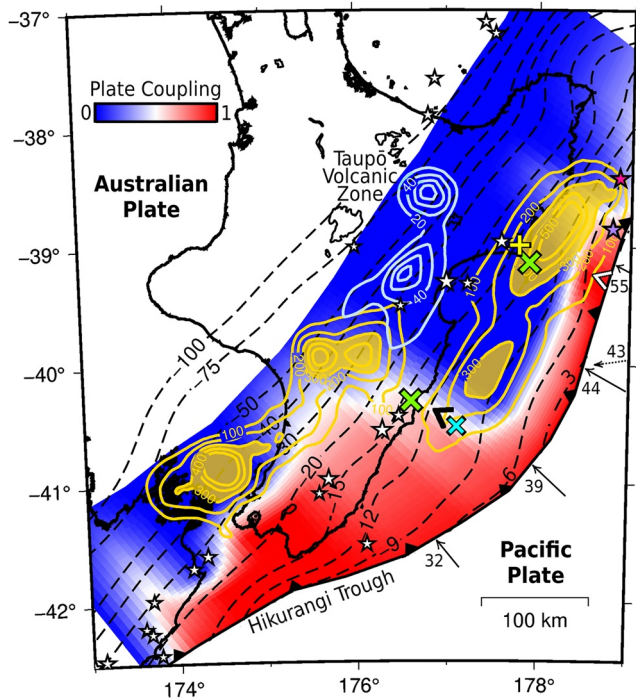
Figure 2. Geophysical setting of the Hikurangi subduction zone. Arrows denote trench-normal convergence rate in units of mm/yr. The dashed arrow shows the plate convergence direction and rate. Colors representing plate coupling coefficient show that the southern Hikurangi margin is effectively locked to 30 km depth (Wallace, Barnes, et al., 2012). Cumulative slow slip events from 2002 to 2014 shown as yellow and blue contours in units of millimeters. Shaded patches highlight cumulative slip greater than 300 mm. Green X's represent inferred deeply subducted seamounts. White stars represent $M > 6$ earthquakes that occurred above 30 km depth in the last 100 years (GeoNet). The pink and purple stars show the epicenters of the 1947 offshore Tolaga Bay and offshore Poverty Bay tsunami earthquakes, respectively (Bell et al., 2014). The blue X shows the location of an inferred fluid source in the subducting slab. Black and white "<" markers represent the approximate locations of Madden Canyon and Poverty Re-entrant, respectively. Yellow "+" shows the location of the Mōrere thermal spring, and corresponding geophysical anomalies. Dashed black lines show depth to the plate interface in units of kilometers (Williams et al., 2013).

Barnes et al., 2010; Bell et al., 2010), and substantial work has been undertaken to understand these subducted seamounts' effects on slip behavior, fluid and sediment transport, and upper plate morphology (e.g., Arai et al., 2020; Barker et al., 2009, 2018; Bell et al., 2014, 2010; Chesley et al., 2021; Zal et al., 2020). These seamounts have been associated with localized uplift of the seafloor, localized positive magnetic anomalies, and are observed to be preceded landward by high-reflectively zones interpreted as underthrusted sediment packages (Bell et al., 2010; Ellis et al., 2015). Typically oblate in shape with footprints on the scale of tens of kilometers, and heights of less than a few kilometers (Barnes et al., 2010; Bell et al., 2010), they have also been linked to the two 1947 tsunami earthquakes that produced some of the largest tsunamis in New Zealand's recorded history (Figure 2; Bell et al., 2014). Although no seamounts subducted further below the North Island have yet been identified using geophysical methods, some have been inferred to exist by other means. For example, tectonic reconstructions based on the Poverty and Ruatoria Re-entrants suggest that very large seamounts have been subducted hundreds of kilometers westward beyond the trench and may currently reside somewhere below the northern North Island (Figure 1; Lewis et al., 1998; Pedley et al., 2010).

The Hikurangi margin presents a rare opportunity to study an active subduction zone with land-based measurements. The subducting Pacific plate is part of a large igneous province, the Hikurangi plateau, and subduction of this relatively buoyant feature has caused much of the forearc region to be exposed subaerially (Litchfield et al., 2007; Nicol et al., 2007). Consequently, the plate interface below the East Coast region is shallow at 12–15 km depth (Figure 2; Williams et al., 2013). Geodetic inversions used to infer plate coupling along the interface suggest that the southern Hikurangi margin is geodetically locked, while the northern portion is creeping aseismically (Figure 2; Wallace, Beavan, et al., 2012; Wallace, 2020). The transition between the two styles of slip occurs across the central margin (Figure 2) with shallow (5–15 km) slow slip events (SSEs) at the northern margin accommodating the majority of expected plate motion where they occur (Figure 2; Wallace, 2020). The cause of along-strike differences at the Hikurangi margin is an ongoing topic of research, and a variety of factors including fluids, seamounts, overriding plate structure, incoming sediment flux, and temperature have been suggested as explanations for the heterogeneous slip behavior observed (Wallace, 2020).

3. Data and Methods

Adjoint tomography is a type of full-waveform inversion that simulates seismic wave propagation by solving the seismic wave equation (Fichtner et al., 2006a, 2006b; Tape et al., 2007; Tromp et al., 2005), and iteratively improves models of Earth structure using the adjoint-state method (Tarantola, 1984). In Chow et al. (2022), we use earthquake-based adjoint tomography to image crustal structure with kilometer-scale resolution by improving a ray-based, 3D tomography model of New Zealand (Eberhart-Phillips et al., 2020). We briefly outline the data and methods here and refer the reader to Chow et al. (2022) for more detailed explanations.

Our starting model is the ray-based NZ-Wide2.2 velocity model of Eberhart-Phillips et al. (2020), which defines P-wave velocity (V_p), the ratio of seismic velocities (V_p/V_s), density, and attenuation (Q_p, Q_s). We define a corresponding V_s model by taking the ratio of the V_p/V_s and V_p models, and extract and interpolate an approximately 475 km by 600 km domain focused on the central North Island, New Zealand (Figure 1). The numerical mesh defining the velocity model explicitly honors topography and bathymetry (Becker et al., 2009) and extends to 400 km depth

The data set consists of 60 geographically well-distributed earthquakes, whose waveforms were recorded on as many as 88 broadband seismometers (Figure 1). Source information and moment tensors are taken from a New Zealand (GeoNet) catalog (Ristau, 2008, 2013) and synthetic seismograms generated using the time-domain spectral element solver, SPECFEM3D Cartesian (Komatitsch & Tromp, 2002a, 2002b). The initial catalog consists of moderate-magnitude ($4.5 \leq M_w < 6.0$), shallow-depth and intermediate-depth ($Z < 60$ km) earthquakes that occurred between 2004 and 2019. We manually select events based on data-synthetic misfit, and perform event declustering to downweight the contributions of clustered events. The recording seismometers include 38 stations from the permanent seismic network of New Zealand (https://www.geonet.org.nz/), and 50 temporary network stations (Figure 1) which provide roughly 8% of the initial data set (Chow et al., 2022), yielding approximately 1,800 unique source-receiver pairs.

We follow the automated inversion procedure outlined by Chow et al. (2020). At each iteration, the data-synthetic misfit for each component (north, east, up) of each source-receiver pair is measured using a windowed cross-correlation traveltime misfit function (Tromp et al., 2005). The adjoint-state method is used to derive the gradient of the misfit function, and an L-BFGS optimization algorithm provides a search direction using a low-rank quadratic approximation to the misfit function (Nocedal & Wright, 2006). The total volumetric gradient is smoothed with a 3D Gaussian to suppress nonuniqueness, with smoothing length and waveform bandpass reduced gradually over the course of the inversion to conservatively approach the global minimum of the misfit function. In total, 28 updates of P-wave and S-wave velocity are performed, with a shortest waveform bandpass of 4–30 s, improving waveform fits with respect to the initial model and introducing P-wave and S-wave velocity changes of up to ±30%.

3.1. Resolution Tests

Point spread functions (PSFs) provide a measure of how point-like perturbations are blurred or smeared by an inversion (Fichtner & Trampert, 2011), and have been used for resolution testing in adjoint tomography studies (e.g., Bozdağ et al., 2016; Tao et al., 2018; Zhu et al., 2015). To perform point spread tests, we perturb our final velocity model **m** by a quantity δ**m**, and attempt to recover the perturbation by solving for the action of the Hessian on the model perturbation (Fichtner & Trampert, 2011). In practice, this is accomplished using finite-differences of gradients

$$\mathbf{H}(\mathbf{m})\delta\mathbf{m} \approx \mathbf{g}(\mathbf{m} + \delta\mathbf{m}) - \mathbf{g}(\mathbf{m}), \tag{1}$$

where $\mathbf{H}(m)$ is the Hessian evaluated at the final model **m**, $\mathbf{g}(m)$ is the gradient evaluated at the final model, and δ**m** is a local model perturbation with respect to the final model. The resulting quantity $\mathbf{H}(\mathbf{m})\delta\mathbf{m}$ is a conservative estimate of the PSF, which provides practical information on the extent of how features in the tomographic model can be interpreted (Fichtner & Trampert, 2011). Here, individual point spread tests define δ**m** to be a 3D spheroidal Gaussian with a peak amplitude equal to 15% of the final V_s model. The size and location of the perturbations are chosen to reflect the specific velocity anomaly being investigated. Computationally, each point spread test requires 2N simulations (N forward and N adjoint), where $N = 60$ is the total number of events. Each simulation is run on 80 cores of the New Zealand eScience Infrastructure's (NeSI's) high-performance computer, named Māui, requiring ∼7,200 core-hours per point spread test.

In Chow et al. (2022), we calculate the Fourier transform of the Hessian at zero wavenumber, or zeroth moment, which conveys how the resolution of the underlying data set varies across the model domain. The zeroth moment test recovers a homogeneous volumetric perturbation in place of δ**m** (Fichtner & Trampert, 2011). In similar fashion to a ray coverage plot, the zeroth moment shows how resolution varies relatively, but does not provide information on resolution length. In Section 4.2, we consider both the zeroth moment test and four separate PSFs, to understand the resolution and robustness with which velocity anomalies located off the east coast of the North Island are modeled.
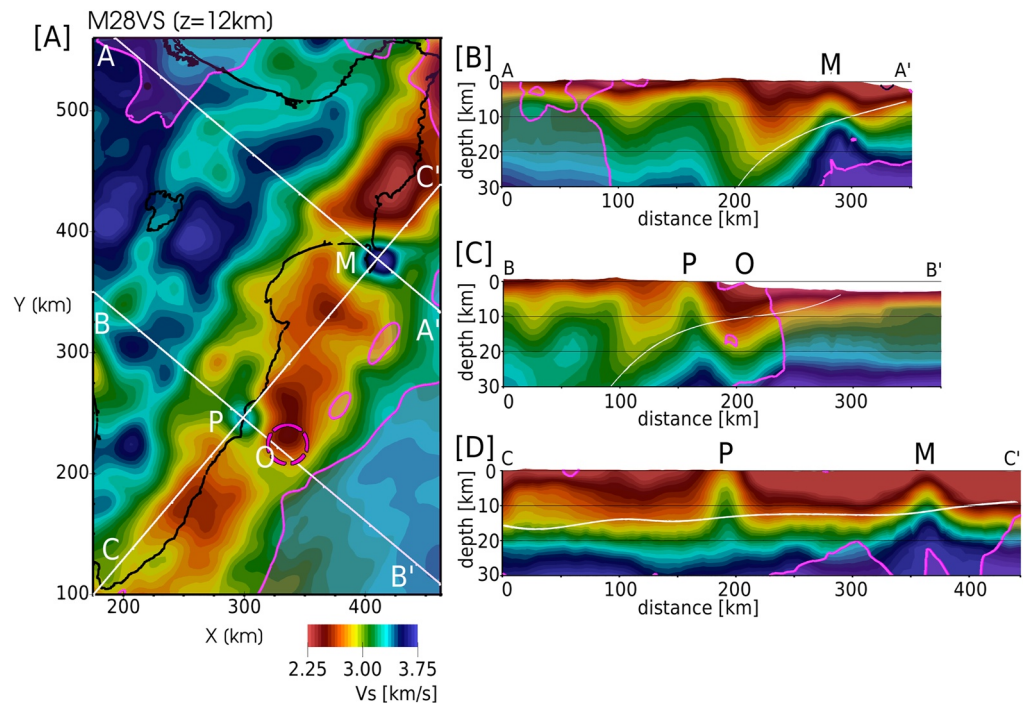
Figure 3. East Coast velocity anomalies shown in V_s. Pink shaded regions highlight the model domain outside the chosen sensitivity threshold, within which model parameters are not interpreted (Figure A2). (a) V_s at 12 km depth showing two localized high-velocity anomalies below Pōrangahau (P) and Māhia Peninsula (M). The low-velocity anomaly offshore Pōrangahau (O) is represented by the dashed pink circle, which corresponds to an outline of the slowest velocities associated with this anomaly at 25 km depth (Figure A1b). Surface traces of cross sections are shown as white lines. (b)–(d) Cross sections through velocity anomalies corresponding to the surface traces shown in (a) at 3× vertical exaggeration. White line shows the plate interface model of Williams et al. (2013).

4. Results

4.1. East Coast Velocity Anomalies

We identify two high-velocity anomalies below the East Coast and a deep offshore low-velocity zone (Figure 3). The high-velocity anomalies are located at approximately plate interface depths (∼12–15 km), below Māhia Peninsula (Feature M; Figure 3) and the North Island township of Pōrangahau (Feature P; Figure 3). The low-velocity zone is located seaward of the Pōrangahau anomaly (Feature O; Figure 3). As shown in Figure 5 of Chow et al. (2022), these anomalies emerge early in the inversion process, suggesting that they are required to reduce long-period data-synthetic misfit. Visualized using a 12-km depth slice through the velocity model (Figure 3a), the high-velocity anomalies appear circular with $V_s > 3.5$ km/s.

The two high-velocity anomalies are distinct with respect to the surrounding velocity structure. In cross-section, they are characterized by bumps of high velocities ($V_s > 3.5$ km/s) centered at interface depths (Figures 3b and 3c). The anomaly below Māhia Peninsula shows a broad region of elevated velocities extending to 20 km depth, almost 10 km below the assumed plate interface (∼12 km; Williams et al., 2013). Above the interface, increased velocities can be seen extending to shallow depths (∼5 km; Figure 3b). The Pōrangahau anomaly has a smaller relative lateral extent, and a more pronounced expression of high velocities extending upwards to the surface (Figure 3c) and below the subduction interface. The two high-velocity anomalies have similar geometries in a trench-parallel cross-section (Figure 3d). About 50 km offshore the Pōrangahau anomaly, a zone of low seismic velocities is visible, corresponding to the offshore low-velocity zone Feature O. Feature O is particularly notable as the most visually prominent difference between initial and final models in the 25 km V_s depth slice (Figure A1b), where it is seen as a roughly 50 km patch of significantly slower ($V_s < 3.5$ km/s) velocities compared to the surrounding region (dashed pink circle in Figures 3a, 4a, and A1b).
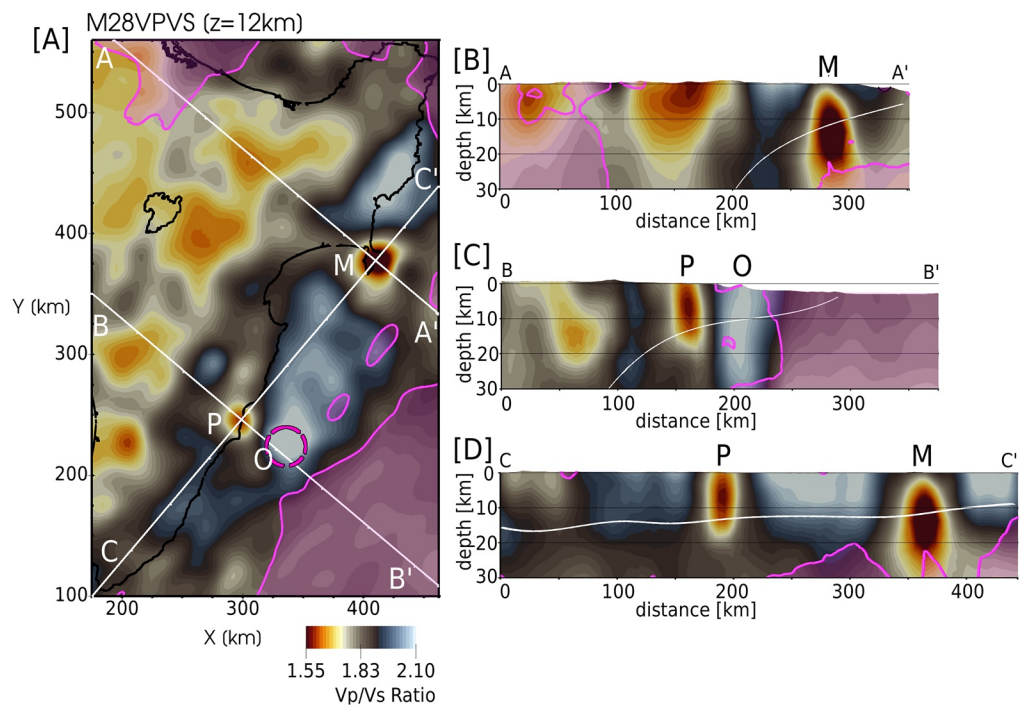
Figure 4. East Coast velocity anomalies in V_p/V_s. Pink shaded regions highlight the model domain outside the chosen sensitivity threshold, within which model parameters are not interpreted (Figure A2). (a) V_p/V_s at 12 km depth showing two localized low-V_p/V_s anomalies below Pōrangahau (P) and Māhia Peninsula (M). The high-V_p/V_s anomaly offshore Pōrangahau (O) is represented by the dashed pink circle, which corresponds to an outline of the slowest velocities associated with this anomaly at 25 km depth (Figure A1b). Surface traces of cross sections are shown as white lines. (b)–(d) Cross sections through high-velocity anomalies corresponding to the surface traces shown in A at 3× vertical exaggeration. White line shows the plate interface model of Williams et al. (2013).

The ratio of seismic velocities (V_p/V_s) is often used to infer the presence of fluids at depth. Due to the higher sensitivity of V_s to the presence of fluids, low V_p/V_s values are commonly used to indicate low fluid content, and vice versa (Audet et al., 2009; Christensen, 1996; Eberhart-Phillips et al., 1989, 2005; Ito et al., 1979). For a Poisson solid (Poisson's ratio = 0.25), the V_p/V_s ratio is equal to 1.73: we use the Poisson's solid as our reference to define high (>1.73) and low (<1.73) V_p/V_s ratios. We define our V_p/V_s model through the direct division of our V_p and V_s models, which may be susceptible to apparent structures arising from differences in model resolution. However, these effects should be small as we are interpreting long-wavelength (~25 km) V_p/V_s structures within a well-sampled region of our model. The two high-velocity anomalies are characterized by low V_p/V_s values (<1.6) surrounded by higher V_p/V_s (>1.8; Figure 4), suggesting lower fluid content compared to the surrounding accretionary prism. The offshore low-velocity zone is more marked, appearing as a high-V_p/V_s feature (>2) adjacent to the Pōrangahau anomaly and coincident with a region of frequent (every 4–5 years) slow slip events (Figure 2; Wallace, 2020). This high-V_p/V_s feature is columnar in shape, extending through the entire 30 km depth range illustrated, suggesting that it may be associated with a source in the subducted oceanic crust.

4.2. Resolution Analysis

We perform a zeroth moment resolution test to determine how robustly imaged these velocity structures are (Chow et al., 2022). Depth slices through the zeroth moment volume are shown in Figure A2, using a threshold value chosen to represent the lateral extent of sensitivity in our velocity model. The threshold region contains all three velocity anomalies to depths of 25 km, meaning our data set is sensitive to velocity heterogeneities in these regions. The pink shaded areas in Figures 3 and 4 show the same threshold value outside of which the updated velocity model is interpretable. In the remainder of this section, we will discuss four separate point spread tests to constrain the resolution of location, size, and shape of the individual anomalies identified in Section 4.1.
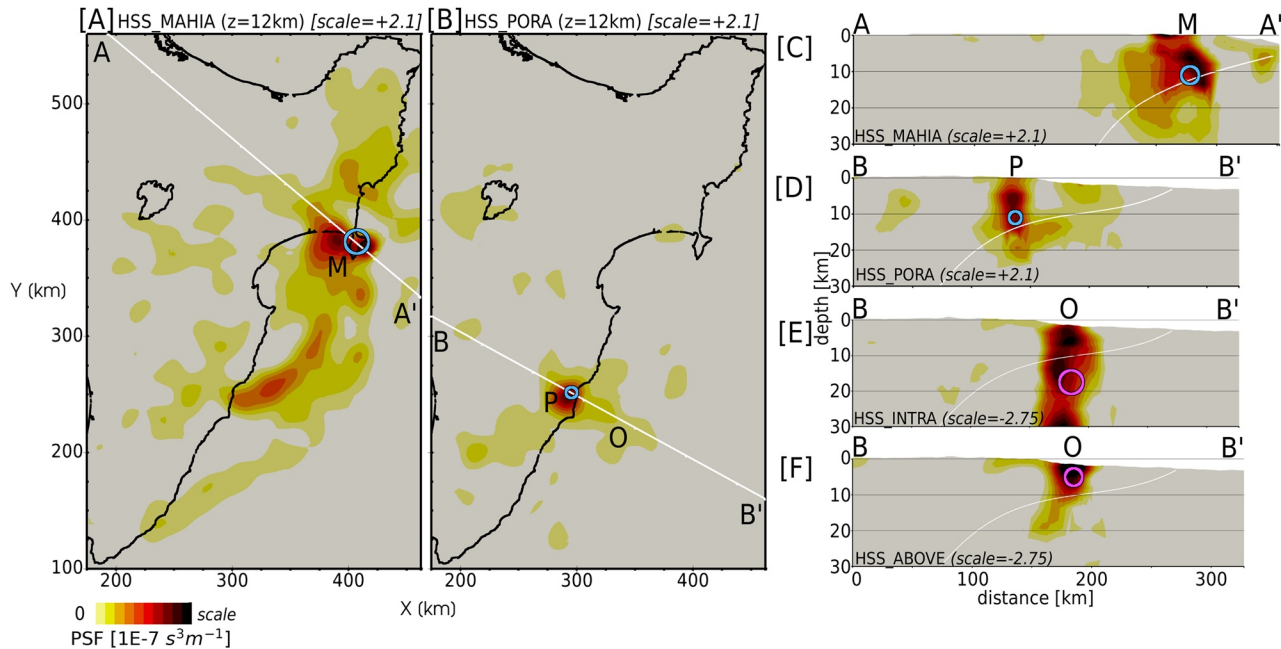
Figure 5. Point spread functions (PSFs) for the Māhia Peninsula (M), Pōranghau (P), and offshore (O) velocity anomalies. Input perturbations are 3D spheroidal Gaussians with peak amplitudes equal to ±15% of the background V_s model. Horizontal (Γ_h) and vertical (Γ_z) full width of the Gaussian perturbations are shown as blue circles for positive perturbations, and pink circles for negative perturbations. (a) Māhia Peninsula PSF ($\Gamma_h = 20$ km); (a–a') trace shown in panel (c). (b) Pōrangahau PSF ($\Gamma_h = 10$ km); (b–b') trace shown in panels (d–f). (c) Māhia Peninsula PSF (a–a') cross section ($\Gamma_z = 5$ km). (d) Pōranghau PSF (b–b') cross section ($\Gamma_z = 3.5$ km). (e) Intra slab low-velocity anomaly PSF ($\Gamma_{h,z} = 21, 7$ km). (f) Above slab low-velocity anomaly PSF ($\Gamma_{h,z} = 15, 5$ km). Note the varying amplitude scale. Cross sections shown at 3× vertical exaggeration. White line in cross sections shows plate interface model of Williams et al. (2013).

The PSF for the Māhia Peninsula anomaly has a complicated geometry (Feature M; Figures 5a and 5c). The peak of the PSF lies a few kilometers offshore from the perturbation itself, indicating uncertainty of a few kilometers in deriving an exact location (Figure 5a). Similarly, lateral smearing over ~100 km suggests that the size of the heterogeneity is not well constrained and that the actual heterogeneity could be smaller than the corresponding velocity signature. Interestingly, the PSF contains a second peak further inland, and a high-amplitude feature to the south, indicating that the updated velocity structure at these locations is affected by heterogeneity beneath the Peninsula. The model shows no corresponding high-velocity anomalies at these locations however (Figure 3), suggesting that this trade-off does not significantly impact the final velocity model. Vertical smearing (Figure 5c) indicates that the heterogeneity affects the inferred velocity structure above and below itself, which suggests that the large vertical extent seen in the V_s and V_p/V_s models is a consequence of the inversion and not a true representation of an anomaly at depth (Figures 3 and 4).

The PSF for the Pōrangahau anomaly (Feature P; Figure 4) shows that the heterogeneity here is more well-resolved, with location uncertainty of a few kilometers (Figure 5b). The PSF also indicates that there is minimal trade-off with the surrounding velocity structure, but lateral smearing means that the width of the velocity anomaly may be larger than the actual heterogeneity. In cross-section (Figure 5d), the peak of the PSF is located a few kilometers above the input perturbation. This may explain the apparent shallow, mid-crustal depth of the Pōrangahau anomaly (Figure 4c), which may be an artifact of the inversion. Conversely, this suggests that the true heterogeneity is likely situated deeper than the corresponding velocity anomaly, and that the shallow, vertically elongated velocity structure is a result of vertical smearing (Figure 5d).

We perform two additional point spread tests to assess the resolution of the offshore low-velocity anomaly (Feature O; Figure 4). The first test attempts to recover a low-velocity anomaly within the subducting slab (Figure 5e). The resulting PSF shows a columnar structure, similar to that observed in V_p/V_s (Figure 4c). To ensure that this columnar structure could not also be the result of a velocity anomaly in the upper plate, we perform a similar test for a low-velocity anomaly input above the plate interface (Figure 5f). The resulting PSF shows that recovery is primarily confined to the upper plate, and consequently implies that the presence of an upper-plate, low-velocity feature would not explain the offshore low-velocity anomaly imaged. In other words, the heterogeneity (Feature O;

Figure 4) is likely an intra-slab low-velocity (high-V_p/V_s) anomaly, whose signature is smeared considerably in the vertical direction (Figure 4c).

Overall, the point spread tests performed for the East Coast velocity anomalies suggest that: (a) the lateral locations of the anomalies are well-resolved, with spatial uncertainties of less than 10 km; (b) the lateral extent of each feature is affected by smearing, but may be roughly estimated by measuring the width of the peak amplitudes of the velocity anomalies; and (c) the vertical extent and exact depths of the features are not well-constrained due to smeared sensitivity of the seismic waves sampling these structures, as well as smoothing in the inversion procedure. The similarity of the PSFs (Figures 5c–5f) to the corresponding V_p/V_s anomalies (Figures 4b and 4c) suggests that the actual high-velocity anomalies lie at interface depths, and that the low-velocity (high-V_p/V_s) offshore anomaly is located within the subducting slab.

4.3. Isosurface Visualization

Isosurfaces connect points of constant value within a volume and are a useful tool for highlighting structures within three-dimensional models. To better visualize the high-velocity anomalies below the East Coast, we investigated various velocity isosurfaces extracted from the V_s velocity model and focus here on a representative example. The selected isosurface defines a constant $V_s = 3$ km/s with vertically exaggerated points colored by depth (Figure 6a). The isosurface is rotated to an oblique, trench-perpendicular viewing angle so that both velocity anomalies are clearly visible.

We choose the value of the isosurface ($V_s = 3$ km/s) to highlight the most prominent segments of the high-velocity anomalies discussed previously, identifiable as yellow colors in Figures 3b–3d. In terms of tectonic structure, this process can be thought of as the stripping away of low-velocity sediments overlying stiffer material such as oceanic and continental crust. This effect is clearly visible in the isosurface as removal of the sedimentary and volcanic cover on the Australian plate and the adjacent accretionary wedge (Figure 6a; Edbrooke et al., 2015). The remaining structures are likely related to basement rocks of the North and South Islands (Mortimer, 2004) and the backstop of the subduction zone forearc (Byrne et al., 1993).

Clearly identifiable in the isosurface are two solitary peaks related to the high-velocity anomalies below Pōrangahau and Māhia Peninsula. Similar to the 2D cross-sections (Figures 3b–3d), the Pōrangahau anomaly is a tall, narrow peak that extends to the surface, while the Māhia Peninsula anomaly features a wide base and lower relative height. Further seaward, a third prominent peak is visible, which spatially correlates with Rock Garden, a known seamount on the incoming Pacific plate (Barnes et al., 2010). Other sections of the isosurface can be linked to known tectonic features of New Zealand. These include a notch in the backstop related to Cook Strait (Lewis et al., 1994), deep depressions related to Taranaki basin (e.g., King & Thrasher, 1996) and Whanganui basin (e.g., Carter & Naish, 1998), and a collection of shallow depressions throughout the Taupō Volcanic Zone (Wilson et al., 1995, 2009). These upper-plate tectonic features are discussed in more detail in Chow et al. (2022).

5. Discussion

5.1. Deeply Subducted Seamounts Below the East Coast

We interpret the East Coast high-velocity anomalies as previously unidentified deeply subducted seamounts located below Pōrangahau and Māhia Peninsula (Figure 1). The 3 km/s isosurface of the velocity model highlights these features and their apparent effect on the velocity structure of the upper crust remarkably well (Figure 6a).

Subduction of partially buried seamounts would have an observable effect on the structure of the accretionary prism and the upper plate, which can be corroborated with known geologic features. Sand table experiments and field observations have been used to predict the effects of subducted seamounts on the upper plate, which include: tectonic erosion at the frontal wedge leading to re-entrant bathymetric features, a complex fracture network that forms in the vicinity of the seamount and is preserved as a permanent furrow or scar, local uplift above the seamount, and increased subsidence in the seamount's wake (Figure 6b; Dominguez et al., 1998, 2000). A recent 3D numerical modeling study investigated the upper-plate crustal deformation effects of subducting seamounts using finite-difference modeling (Ruh et al., 2016). The results of that study agree with the analog predictions, and also provide useful quantification of the heterogeneous stress state within the upper plate, which we can use to examine slip behavior adjacent to subducted seamounts (Section 5.3).
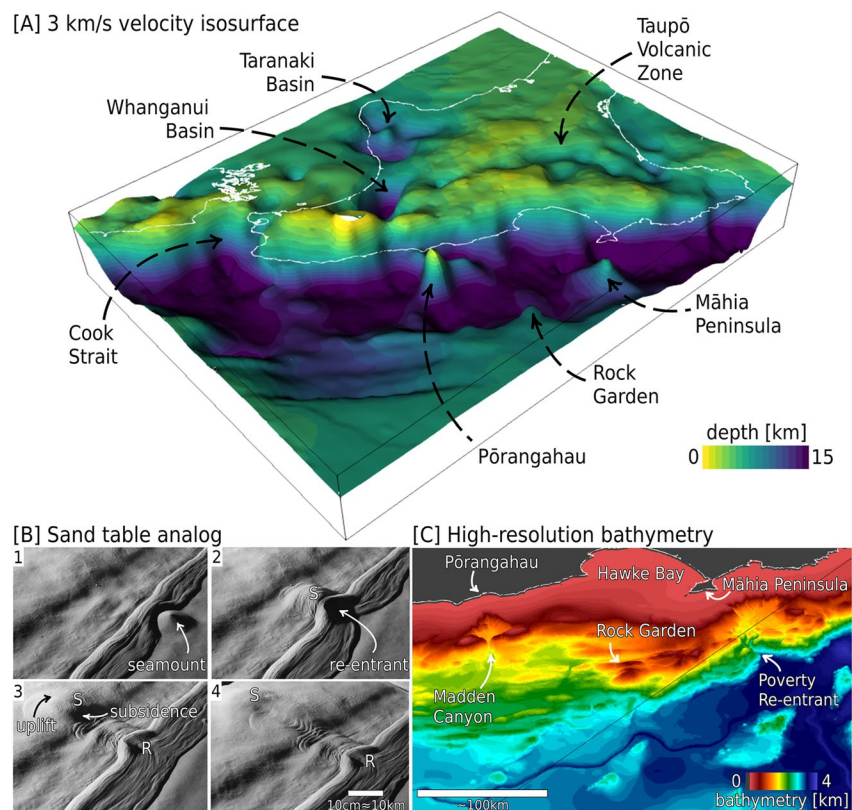
Figure 6. Evidence for deeply subducted seamounts below the East Coast. (a) Isosurface for V_s = 3 km/s colored by depth and vertically exaggerated. Anomalies related to the two inferred seamounts below Pōrangahau and Māhia Peninsula are visible as peaks that likely represent expressions of the seamounts on the upper plate. Also visible is a peaked anomaly related to the known seamount at Rock Garden (c). (b) Seamount subduction represented by an analog sand table experiment, modified from Dominguez et al. (1998). Panels represent increasing time: b1) The seamount (S) indents the inner trench slope; b2) A shadow zone forms in the wake of the seamount. The re-entrant (R) is affected by intense mass-sliding; b3) The seamount is subducted further, with local uplift above the seamount, and subsidence in its wake; b4) Extension occurs in the wake of the seamount, leading to a subsided area behind the crest of the seamount. A permanent fracture network is left in the upper plate. (c) Offshore East Coast bathymetry showing the relative locations of inferred seamounts and bathymetric features (Mitchell et al., 2012).

Due to smearing and smoothing effects in our inversion, it is difficult to directly measure the size and subduction depth of the two inferred seamounts. Depending on their actual shape and aspect ratio, the full extent of a seamount may fall below the resolution limit of the tomographic inversion, while horizontal smoothing may smear the anomalies laterally (Figure 5). Similarly, based on the results from the point spread tests (Section 4.2), the height of the velocity anomalies is not well-constrained. It is likely that the height of the velocity anomalies does not directly correspond to the height of the inferred seamounts, but rather represents a blurred image of an anomaly at depth.

To examine whether the inferred seamounts have similar geometric characteristics to known seamounts at the Hikurangi margin, we can compare to interpretations of offshore active source data. For example, Barker et al. (2018) interpreted seismic reflection data spanning a seamount offshore Poverty Bay, revealing a lozenge-shaped ridge 40 km long, 15 km wide, and of up to 2.5 km relief, which provides a first-order constraint on the size of the seamounts suggested here. We note, however, that this well-studied region in the northern Hikurangi—which contains seamounts linked to the 1947 tsunami earthquakes offshore Tolaga Bay and Poverty Bay (Figure 2; Bell et al., 2014)—lies outside our model domain (Figure 1).

5.1.1. Māhia Peninsula Seamount

We propose that a large seamount has been subducted below Māhia Peninsula. We estimate the lateral extent of this Māhia Peninsula velocity anomaly at 25 km based on its V_p/V_s signature, which agrees with the size of

known offshore seamounts elsewhere on the Hikurangi subduction margin. We presume that a seamount originally attached to the incoming plate would now sit at plate interface depth, which is approximately 12 km depth (Williams et al., 2013). Based on a distance to the trench of approximately 100 km and a margin normal convergence rate of 55 mm/yr (Figure 2), this inferred seamount would have first impinged on the margin approximately 1.8 Ma. In this section, we present independent evidence that supports this interpretation.

The Poverty Re-entrant northeast of Māhia Peninsula has been interpreted as a seamount scar resulting from consecutive seamount impacts over the last 1–2 Myr (Figure 6c; Collot et al., 1996; Lewis & Pettinga, 1993; Lewis et al., 1998; Pedley et al., 2010). Based on relative locations and the plate convergence direction, it is likely this re-entrant is associated with the Māhia Peninsula seamount. The Poverty Re-entrant has previously been identified as a double feature consisting of lower and upper indentations (Collot et al., 1996). The geometry of the lower indentation (i.e., steep-sided, "V"-shaped deflection of the frontal wedge) is suggestive of a re-entrant, while the morphology of the upper indentation indicates eastward subsidence and subsequent canyon erosion (Collot et al., 1996). The upper Poverty indentation has been linked to subsidence and drainage development in the wake of a very large seamount (Pedley et al., 2010), which we propose may be the Māhia Peninsula seamount imaged here. Topographic uplift would similarly be expected for a seamount below land, and may explain the anomalous topographic high of Māhia Peninsula with respect to the surrounding coastline (Figure 6c).

Other studies have inferred the presence of a deeply subducted seamount near Māhia Peninsula. The offshore Lachlan fault system (Figure 1) has undergone almost 6 km vertical separation of its northern segment with respect to its southern extent, which Barnes et al. (2002) hypothesized to be the upper-plate response to a subducted seamount >10 km below the Peninsula. Approximately 20 km landward of Māhia Peninsula, the Mōrere thermal spring (Figure 1) is one of only two thermal springs in this region, whose chemical signature shows enrichment in mantle components suggesting that high-permeability paths extend from the subducted plate to the surface (Reyes et al., 2010). The coincident Mōrere magnetic anomaly has been linked to a seamount subducted within the last 2 Myr (Figure A3; Hunt & Glover, 1995), which agrees with previous associations of positive magnetic anomalies with locations of offshore seamounts (Bell et al., 2010). Hunt and Glover (1995) proposed that these magnetic anomalies could be caused by either shallowly buried ophiolite bodies detached from the subducting plate, or by Cretaceous seamounts on the upper part of the subducting plate (Figure A3c); our results are consistent with the latter interpretation.

Below the Mōrere thermal spring, ray-based tomography revealed a high-V_p anomaly at approximately 8 km depth, which was suggested to be volcanic in origin (Eberhart-Phillips et al., 2015). Magnetotelluric studies here show a conductive patch on the plate interface, with a more resistive patch below the Peninsula (Heise et al., 2017). The conductive patch was interpreted to indicate the presence of fluid- or clay-rich sediments, and may be related to underthrust, fluid-rich sediments at the leading flank of the seamount, similar to those proposed for offshore seamounts at the northern Hikurangi margin (Bell et al., 2010). The Mōrere anomalies roughly coincide with the inferred Māhia Peninsula seamount, and may thus correspond to its down-dip extent, or to the upper crust's response to such a geometric heterogeneity.

5.1.2. Pōrangahau Seamount

We propose that a previously unrecognized seamount has been subducted almost 100 km beyond the trench and now lies below the East Coast township of Pōrangahau. From the V_p/V_s signature (Figure 4), this inferred Pōrangahau seamount has an approximate lateral extent of 15 km, agreeing with the size of known offshore seamounts further north. The seamount is inferred to lie at a plate interface depth of 15 km (Williams et al., 2013). A back-of-the-envelope calculation based on a margin normal convergence rate of 39 mm/yr (Figure 2; Wallace, 2020) and distance to the trench of 150 km (Figure 1), suggests that the Pōrangahau seamount first impacted the trench ~4 Ma.

A distinctive bathymetric feature in the vicinity of the Pōrangahau seamount is Madden Canyon (Figure 6c). Although it is too far from the trench (~100 km) to be easily explained as a re-entrant, Madden Canyon may have formed as an area of subsidence in which mass sliding and canyon erosion was promoted at the trailing flank of the Pōrangahau seamount (Figure 6c; Dominguez et al., 1998; Ruh et al., 2016). There is no obvious re-entrant feature in the bathymetry data related to the Pōrangahau seamount (Figure 6c), but rapid growth of the accretionary pile at the central Hikurangi margin may have obscured such a feature (Von Huene & Scholl, 1991). Similarly, there is no corresponding topographic high, like that represented by Māhia Peninsula, which may indicate that

the Pōrangahau seamount lies at a deeper interface depth or has smaller relief (or both) than the Māhia Peninsula seamount. Limited evidence corroborating the presence of the Pōrangahau seamount may also reflect a lack of targeted geophysical studies in this region.

Other potentially relevant differences between the two inferred seamounts that are not well constrained by our results include: the differing characteristics of the accretionary prism, the size and aspect ratio of each seamount, and their respective burial depths prior to subduction. In contrast to the Māhia Peninsula seamount, if the Pōrangahau seamount is smaller, was more deeply buried on the incoming plate before impact at the trench, has been subducted to deeper depths, or some combination of the three, its magnetic and topographic signatures will likely be more subdued. Partial decapitation and subsequent underplating of the seamount, a process which has been suggested to occur at other subduction zones (Cloos & Shreve, 1996; Prendergast & Offler, 2012), may also explain the lack of external evidence, and is supported by the presence of volcanic-sedimentary deposits identified along the East Coast (Kobe & Pettinga, 1984; Pettinga, 1982). It is also possible that other subduction-related tectonic features can manifest the imaged high-velocity anomalies. For example, imbricated thrust faults will lead to unexpectedly fast velocities at depth; however, these should form linear structures rather than the point-like anomalies we image (Figure 6a). Similarly Hunt and Glover (1995) suggested that shallowly buried ophiolite bodies, similar to the high-velocity Matakaoa volcanics to the north (Eberhart-Phillips & Bannister, 2015), are another potential source for positive magnetic anomalies observed at the northern Hikurangi margin. However, the size and location of these velocity anomalies, and spatially correlated geophysical and geological evidence, strongly support our interpretation of deeply subducted seamounts.

5.2. Intraslab Fluid Source

We interpret the low-V_s, high-V_p/V_s, Feature O (Figure 4c) identified offshore Pōrangahau, as an intraslab fluid source within the downgoing plate. The 25 km depth slice of the final V_s model (Figure A2f) shows that this slow anomaly is within the resolution limit of our data set. The PSF tests provide a convincing argument that the observed V_p/V_s signature (Figure 4c) is best explained by a vertically smeared, slow anomaly below the predicted interface (Figure 5e). If located within the slab, this deep, low-velocity signature may correspond to a hot plume-like structure from below, but its location within a subduction setting, its high-V_p/V_s signature, and spatial correlation with the Pōrangahau seamount and repeating slow slip events (Figure 2), suggest this anomaly originates from intraslab fluids.

Fluid within faulted slab material has been inferred to exist in several subduction zones, and used to explain anomalous slip behavior at the Hikurangi margin. For example, using electrical resistivity measurements at the northern Hikurangi margin, Chesley et al. (2021) imaged a subvertical conductor that cuts through the western flank of Tūranganui Knoll (Figure 1), interpreted from seismic reflection data to indicate normal faulting on either side of the seamount (Barnes et al., 2020). Chesley et al. (2021) explained the low resistivity of this anomaly as a fault that acts as a porous conduit for fluid flow, showing similar features to bending-induced normal faults at the Middle America Trench that are thought to allow fluid to permeate into the oceanic crust and upper mantle (Naif et al., 2015; Ranero et al., 2003). They also suggested that a lack of sediments above Tūranganui Knoll may permit a more direct pathway for fluid infiltration into the fault. If this interpretation is also applicable to the low-velocity feature we have imaged (Feature O), it would support the hypothesis that this feature is a similar bending-induced, fluid-filled fault structure adjacent to the Pōrangahau seamount.

5.3. Implications for Seismic and Aseismic Behavior

Seamounts entering the Hikurangi subduction zone have previously been identified close to the trench and thus in the early stages of subduction. Recognition in this study of the Māhia Peninsula and Pōrangahau subducted seamounts may help to explain anomalous seismic and aseismic behavior observed close to their respective locations. As mentioned above, numerous factors have been proposed as explanations for variations in coupling coefficient along the Hikurangi megathrust interface. One such interpretation suggests that permeability variations in North Island terrane blocks results in heterogeneous fluid distribution on the interface, leading to the observed variations in plate coupling (Reyners et al., 2017). Based on our findings, we instead suggest that the inferred seamounts at Māhia Peninsula and Pōrangahau may play a more direct role in along-strike variations in plate coupling.

Numerical experiments of seamount subduction provide insight into the physical consequences of this process. Ruh et al. (2016) used 3D finite-difference models to investigate upper-plate crustal deformation in response to seamount subduction. Under most conditions, their model predicts high tectonic overpressure in the upper plate in front of a subducted seamount, and tectonic underpressure above and at its trailing edge. In comparison to observations at the Costa Rica margin, Ruh et al. (2016) concluded that: (a) the heterogeneous stress field around subducted seamounts and the deformation of the upper plate act together as a barrier for earthquake ruptures starting from smooth parts of the plate interface, and (b) highly stressed areas near a seamount can trigger earthquakes with large stress drop but small rupture surface. Sun et al. (2020) performed finite element modeling of seamount subduction and concluded that sediment overconsolidation on the leading flanks of seamounts results in fracturing of the upper plate and increased tectonic compression and yield strength, favoring the storage of elastic strain and seismic behavior. In contrast, underconsolidation in the stress shadow of the seamount is suggested by that work to result in increased porosity, decreased tectonic compression, and preferentially aseismic behavior such as slow slip (Figure 7b). The numerical studies undertaken by Ruh et al. (2016) and Sun et al. (2020) paint a picture of subducted seamounts capable of hosting small earthquakes in their immediate vicinity, while otherwise promoting aseismic behavior up-dip and even acting as barriers to the rupture of large earthquakes originating elsewhere on the interface.

Pōrangahau and Māhia Peninsula are both areas of anomalously high rates of clustered seismicity, which may be manifestations of the small-to-moderate-sized earthquakes predicted at the leading edge of subducted seamounts (Ruh et al., 2016; Sun et al., 2020). Pōrangahau has seen episodes of moderate-magnitude swarm seismicity (Jacobs et al., 2016) and repeated earthquakes (Pita Sllim, 2021), and moderately sized earthquakes accompanying geodetically observed SSEs (Figure 7c; Wallace, Beavan, et al., 2012). At Māhia Peninsula, triggered microseismicity has been temporally correlated with shallow SSEs in the region, clustered near the Peninsula (Figure 7d; Delahaye et al., 2009). Comparisons can be drawn with the offshore seamounts at the northern Hikurangi (Figure 1), which have been linked to the two 1947 offshore-Gisborne earthquakes (Bell et al., 2014). These two earthquakes shared many similarities with the tsunami earthquake defined by Kanamori (1972), which produces an anomalously large tsunami for its magnitude. The spatial coincidence of the 1947 earthquakes' epicenters with identified seamounts implies that seamounts can host moderate-sized earthquakes in their immediate vicinity, but it is difficult to take the comparison further as these seamounts are much closer to the trench, and not as deeply subducted. Further work is needed to draw connections between faulting mechanisms, earthquake depths, and these inferred seamount locations.

Geodetic observations show that the locked-to-creeping transition on the Hikurangi plate interface extends approximately NW-SE through the central Hikurangi margin, perpendicular to the trench axis and almost directly through Pōrangahau and the offshore low-velocity anomaly (Figure 2; Wallace, 2020). The margin further south is interpreted to be more geometrically and compositionally uniform, enabling broader zones of locking, whereas further north shallow SSEs accommodate most relative plate motion aseismically (Wallace, 2020). Interestingly, the spatial extent of the largest slip related to these shallow northern SSEs is segmented near Hawke Bay, with a southern terminus just south of Pōrangahau (Figure 7a). This segmentation roughly correlates with the locations of the two deeply subducted seamounts and may be linked to the affected upper-plate regions surrounding each seamount (dashed blue circles; Figure 2).

Several theories have been posited to link seamounts with megathrust slip behavior. Based on the locations of our two seamounts in a predominantly aseismic patch of the plate interface (Figure 2), our findings are consistent with the idea put forth by Wang and Bilek (2011) that describes seamounts as geometric irregularities impinging on the upper plate. According to this interpretation, seamounts must break through upper plate rocks to accommodate plate convergence and, at low temperatures corresponding to shallow seismogenic depths, this results in fracturing of the accretionary wedge and upper plate, and to a lesser degree the seamount itself. Between the point at which a seamount initially enters the trench and the depths at which mantle viscosity becomes relevant, these seamounts are expected to damage their surroundings brittlely, leaving a permanent scar in their wake that is less able to accumulate elastic strain necessary for coseismic rupture propagation (Bangs et al., 2006; Cummins et al., 2002; Wang & Bilek, 2011).

We propose that repeated seamount subduction at the northern Hikurangi margin has resulted in a region of extensive upper plate fracturing (Figure 7a). In contrast, any seamounts entering the southern margin are likely buried under several kilometers of sediments (Barnes et al., 2010), which may suppress their ability to affect
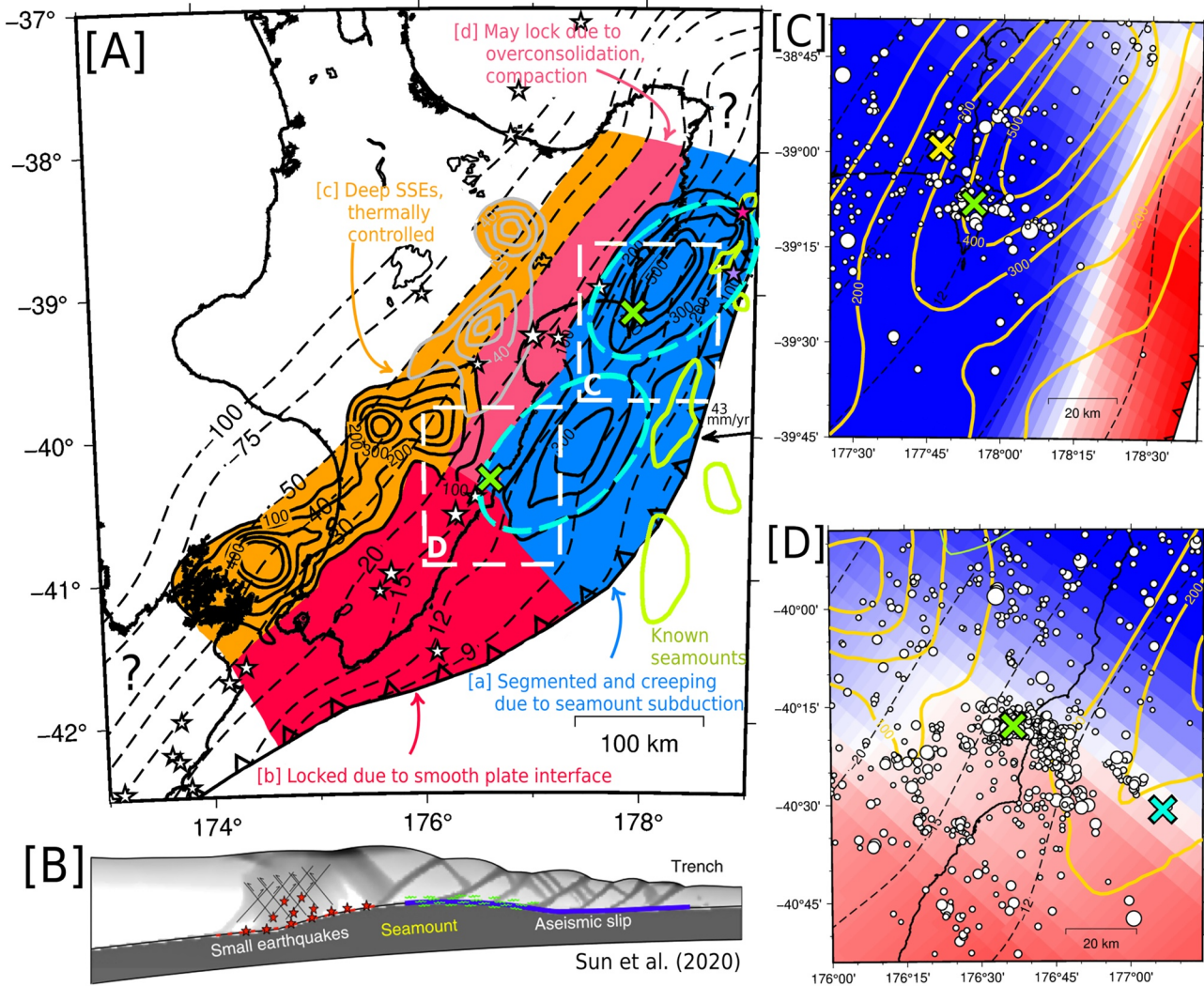
Figure 7. Subducted seamounts (green X's) and seismic and aseismic behavior observed at the Hikurangi subduction margin. (a) Possible segmentation of the plate interface, controlled by rough crust subduction at the northern and central Hikurangi margins, in contrast to smooth plate interface at the southern margin. Spatial segmentation of shallow slow slip events highlighted by blue dashed ovals. White stars represent shallow (<30 km depth), $M > 6$ earthquakes that have occurred in the last 100 years (GeoNet). The pink and purple stars show the epicenters of the 1947 offshore Tolaga Bay and offshore Poverty Bay tsunami earthquakes, respectively (Bell et al., 2014). (b) Cartoon cross section of a subduction zone showing expected slip behavior and upper plate faulting during seamount subduction from Sun et al. (2020). (c) Māhia Peninsula seamount seismic and aseismic behavior. Earthquakes between 2000 and 2021, $M > 2.5$ at 1 km below or 4 km above plate interface depths (Williams et al., 2013) shown as white circles. Mōrere thermal spring shown as yellow X. (d) Pōrangahau seamount seismic and aseismic behavior. Blue cross shows location of inferred intraslab fluids.

upper plate morphology, allowing the interface to lock (Figure 7b; Wallace, 2020). This line of argument has previously been unable to account for the location of the locked-to-creeping transition at the central Hikurangi margin, because the central margin features a more well-developed accretionary wedge than the northern margin, producing a smooth incoming seafloor that is more straightforwardly reconcilable with a locked interface (Wallace, 2020). However, with the recognition of a seamount below Pōrangahau, we suggest that Pōrangahau may represent the southern extent of partially buried seamounts that are able to significantly influence the mechanical integrity of the upper plate. Along-strike cross sections through our V_s and V_p/V_s models corroborate this interpretation, showing lower velocities and higher V_p/V_s values north of Pōrangahau, which may be interpreted as a more damaged upper plate with respect to the locked southern Hikurangi margin (Figure A4). Trench-fill sediment thickness is up to 5 km offshore Cook Strait at the southern Hikurangi margin (Barnes et al., 2010), whereas further north it thins to less than 1 km and seamounts are almost fully exposed on the incoming plate (Figure 1). This gradient in sediment thickness near Pōrangahau may represent a critical region where sediment

thickness and seamount heights exchange roles as the dominating seafloor feature affecting slip behavior on the interface (Figure 2).

The inferred intraslab fluid source offshore Pōrangahau may also play a role in SSE timing and location. Warren-Smith et al. (2019) proposed that episodic release of fluid pressure from the overpressured subducting crust into the upper plate influences the timing of SSEs on the megathrust. Our inferred intraslab fluid source is located below the southern end of a region experiencing SSEs every 4–5 years (Figure 7d; Wallace, 2020), supporting the idea that accumulation and release of fluid pressure across the plate interface has a spatio-temporal influence on slow slip events (Warren-Smith et al., 2019). The spatial proximity of the inferred fluid source to the Pōrangahau seamount (<50km) suggests a connection between the two anomalies (Figure 2). Assuming the interpretation of Warren-Smith et al. (2019) also applies to SSEs offshore Pōrangahau, we suggest that these pressure cycling episodes may be preferred adjacent to seamounts, where fluid-filled bending-induced normal faults have been observed (Barnes et al., 2020; Chesley et al., 2021). Similarly, if the upper plate is left damaged in the wake of a subducting seamount (Wang & Bilek, 2011), it may provide preferential pathways for fluids to travel across the interface and into the upper plate. Given this interpretation, however, it remains unclear why we do not image a similar low-velocity (high-V_p/V_s) feature adjacent to the Māhia Peninsula seamount.

6. Conclusions

We identify velocity anomalies below the east coast of the North Island of New Zealand using a newly derived adjoint tomography velocity model presented in detail in a companion paper (Chow et al., 2022). PSFs are used to constrain the robustness of these features, showing that they are well resolved, although smearing in the inversion procedure increases the uncertainty of their sizes and shapes.

The two high-velocity anomalies are interpreted as previously unidentified, deeply subducted seamounts below Māhia Peninsula and Pōrangahau. We also interpret a distinctive low-velocity (high-V_p/V_s) anomaly as an intraslab fluid source, potentially related to fluid-filled, bending-induced normal faults. The approximate size and location of the two seamounts are consistent with those of known offshore seamounts, and with the existence of bathymetric features predicted by analog sand table experiments and numerical simulations. We propose the Poverty Re-entrant to be both the re-entrant and associated subsidence feature related to subduction of the Māhia Peninsula seamount, which would have first impacted the trench ~2 Ma. The anomalous topographic high of the Peninsula is also linked to predicted topographic uplift above the inferred seamount. We propose that Madden Canyon is a corresponding subsidence feature related to the Pōranghau seamount, which first impacted the trench ~4 Ma, based on modern plate convergence rates. Corroborating evidence for the presence of the Pōrangahau seamount is more limited, but features such as a magnetic anomaly, re-entrant, or topographic uplift, may be obscured due to its differing age, size, or location relative to the Māhia Peninsula seamount.

Anomalous seismic and geodetic phenomena observed at Pōranghau and Māhia Peninsula—including swarm seismicity, magnetic anomalies, and a solitary thermal spring west of Māhia Peninsula—are plausibly explained by the existence of deeply subducted seamounts. Plate coupling and shallow SSEs inferred from geodetic observations and inversions also correlate well with the locations of these seamounts. The inferred intraslab fluid source offshore Pōrangahau is imaged below a region of frequent, shallow SSEs, and its location is in agreement with previous ideas linking the release of fluid pressure from the downgoing plate with the timing of SSEs. We suggest that this fluid source may be fluid-filled, bending-induced normal faults within the downgoing slab.

Based on these findings, we suggest that the upper plate at the Hikurangi margin is left extensively fractured in the wake of each subducting seamount, rendering it less capable than otherwise of storing elastic strain. We propose that upper plate damage can account for the observed differences in along-strike properties of the Hikurangi subduction zone, provides a possible explanation for the locked-to-creeping transition zone and segmentation of shallow SSEs observed, and may mitigate the extent and effects of future large subduction zone earthquakes.

Appendix A

Figures A1 and A2 are modified versions of counterparts included in the companion paper (Chow et al., 2022). We include these here to indicate the source of two specific features included in Figures 3 and 4. These include (a) the notable low-velocity anomaly offshore Pōrangahau, represented by a dashed pink circle in Figure A1b, and (b) the sensitivity threshold derived from the zeroth moment test, represented as the pink outline in Figure A2.

Figures A3 and A4 are included to provide additional evidence for main text figures. The Mōrere magnetic anomaly, which is marked on Figures 1 and 2, is shown in more detail and alongside the adjacent Māhia Peninsula velocity anomaly in Figure A3. In Figure A4 we show trench-parallel cross sections of the velocity model in support of the proposed spatial segmentation of the Hikurangi subduction margin illustrated in Figure 7.
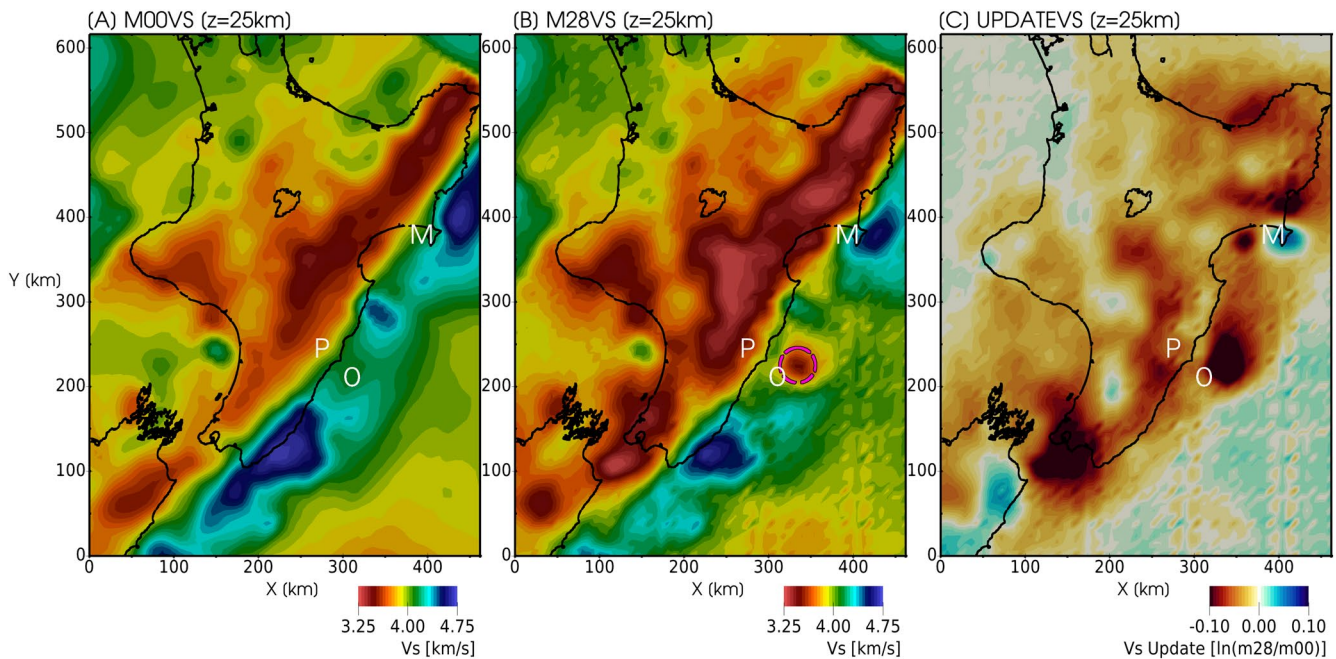
Figure A1. Comparisons of initial (M00; left) and final (M28; center) V_s velocity models at 25 km depth, alongside the net model update (ln(M28/M00); right), highlighting the offshore low-velocity anomaly (Feature O). The dashed pink line in Panel B roughly outlines the slowest velocity associated with this anomaly. Locations of the high-velocity anomalies below Pōrangahau (Feature P) and Māhia Peninsula (Feature M) also shown. Numerical artifacts related to mesh coarsening layers are visible in the final velocity model and net model update, discussed in Chow et al. (2022).
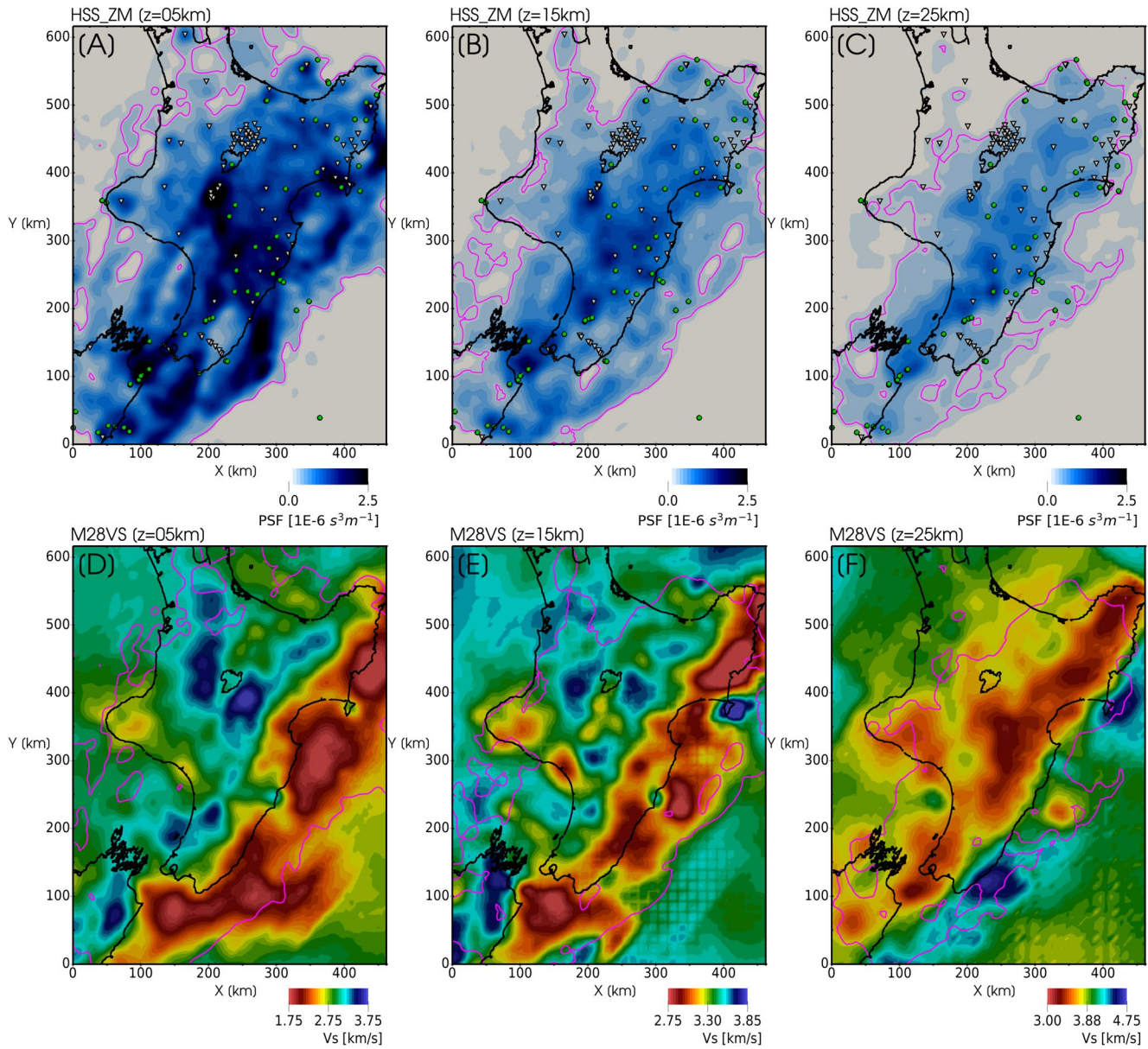
Figure A2. Zeroth moment point spread function (PSF) defining spatial sensitivity of the data set used to derive our velocity model. The pink line corresponds to a threshold value of $2E-7$ s^3 m^{-1}. Velocity heterogeneities located in regions below the threshold have limited to no sensitivity and are consequently not interpreted. (a–c) Depth slices through the zeroth moment PSF at 5, 15, and 25 km depth. Green circles and inverted triangles denote sources and receivers used in the inversion, respectively. (d, e) Depth slices through our V_s velocity model at 5, 15, and 25 km depth. Pink lines are the same as those shown in (a–c).
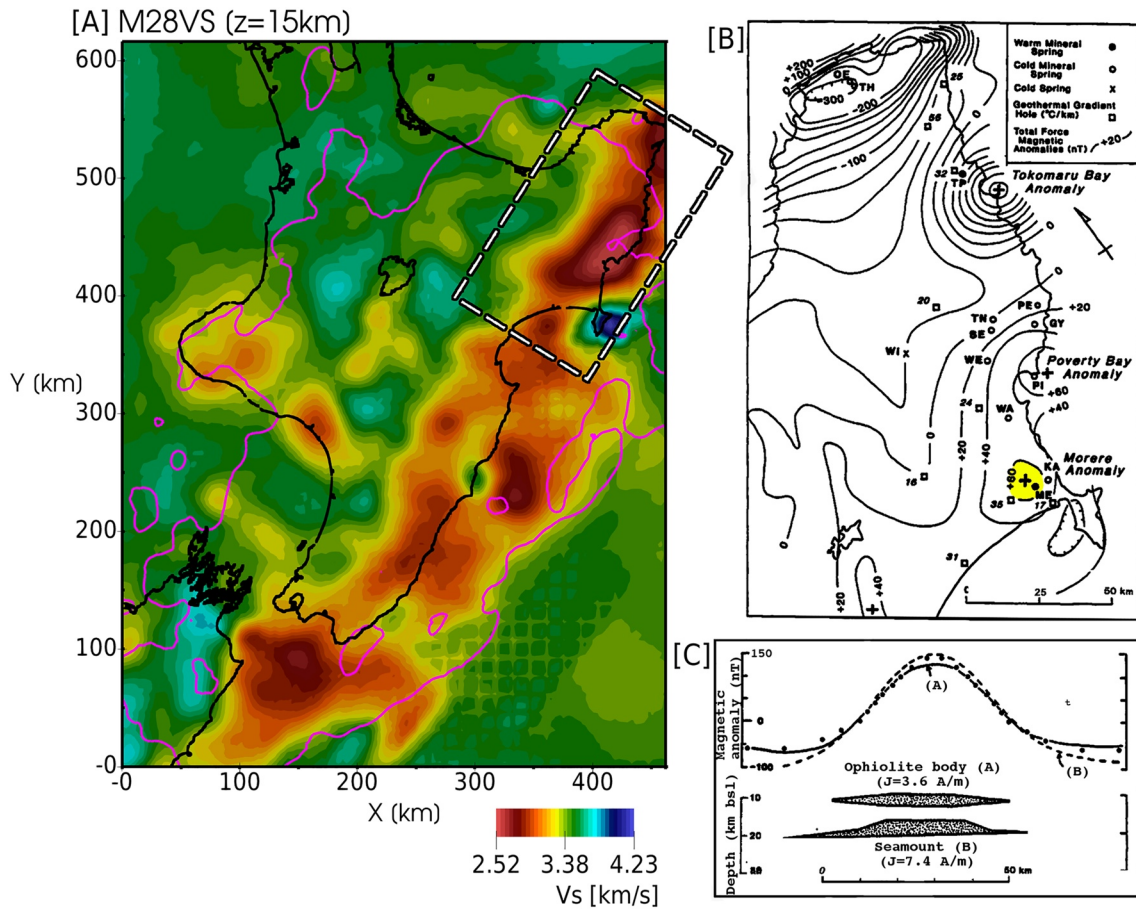
Figure A3. A comparison of the Māhia Peninsula high-velocity anomaly, and the previously identified Mōrere magnetic anomaly from Hunt and Glover (1995). (a) Final velocity model V_s at 15 km depth. The pink line shows the threshold value of the zeroth moment test, denoting the region in which our data set is sensitive to velocity changes. The dashed white line approximately outlines the boxed region in (b). (b) Magnetic anomaly map showing total force anomalies at 3 km above sea level, alongside thermal gradient data and known mineral springs. The yellow highlighted region denotes the Mōrere magnetic anomaly. Slightly modified from Figure 3 of Hunt and Glover (1995). (c) Observed (open circles) and synthetic (solid and dashed lines) magnetic anomalies through an east-west profile of the Tokomaru Bay anomaly shown in (b). The magnetic bodies used to calculate the synthetic anomaly profiles are shown below. Slightly modified from Figure 4 of Hunt and Glover (1995).
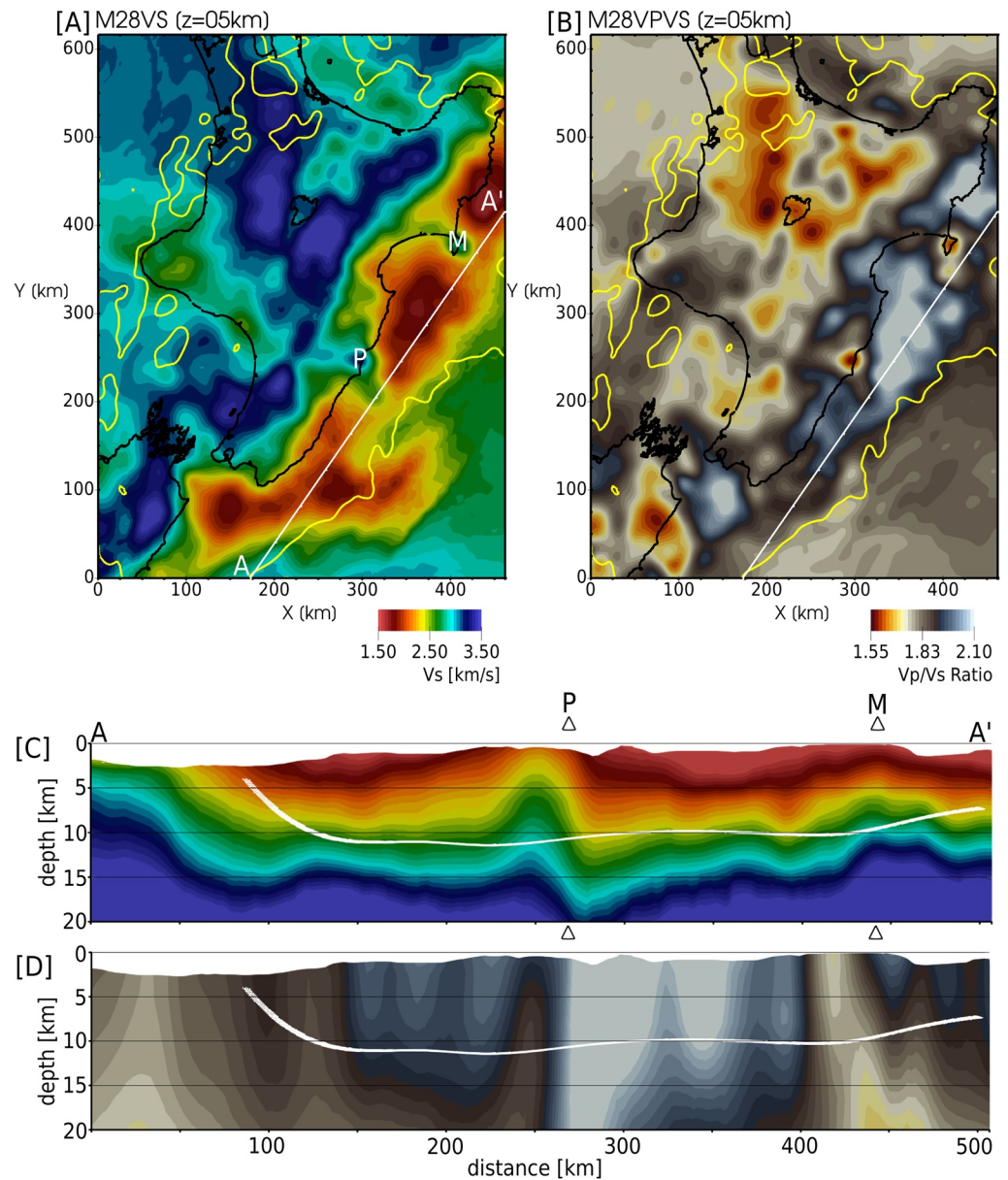
Figure A4. Shallow depth slices and along-strike cross sections through the final V_s and V_p/V_s models highlighting upper plate crustal heterogeneity. (a) Final velocity model at 5 km depth. White line shows the surface trace of the cross sections shown in (c) and (d). Features P and M correspond to Pōrangahau and Māhia Peninsula, respectively. Yellow line denotes the region within a sensitivity threshold where model parameters can be interpreted (Figure A2). (b) Final V_p/V_s model at 5 km depth. (c) Final V_s model along (a–a') shown in (a). Triangles show relative locations of P and M shown in (a). Same color scale as (a). (d) Final V_p/V_s model along (a–a'). Same color scale as (b). This figure illustrates the heterogeneous upper plate velocity structure north and south of Pōrangahau, indicating a more damaged upper plate in the northern Hikurangi margin.

Data Availability Statement

The adjoint tomography velocity model analyzed in this study is publicly available through the IRIS Earth Model Collaboration (EMC) repository (https://doi.org/10.17611/dp.emc.2021.nzatomnnorthvpvs.1). References to the data used to derive this velocity model can be found in the following intext citation reference: Chow et al. (2022).

References

Arai, R., Kodaira, S., Henrys, S., Bangs, N., Obana, K., Fujie, G., et al. (2020). Three-dimensional P wave velocity structure of the Northern Hikurangi margin from the NZ3D experiment: Evidence for fault-bound anisotropy. *Journal of Geophysical Research: Solid Earth*, *125*(12), e2020JB020433. https://doi.org/10.1029/2020jb020433

Audet, P., Bostock, M. G., Christensen, N. I., & Peacock, S. M. (2009). Seismic evidence for overpressured subducted oceanic crust and megathrust fault sealing. *Nature*, *457*(7225), 76–78. https://doi.org/10.1038/nature07650

Bangs, N. L., Gulick, S. P., & Shipley, T. H. (2006). Seamount subduction erosion in the Nankai Trough and its potential impact on the seismogenic zone. *Geology*, *34*(8), 701–704. https://doi.org/10.1130/g22451.1

Barker, D., Henrys, S., Caratori Tontini, F., Barnes, P. M., Bassett, D., Todd, E., & Wallace, L. (2018). Geophysical constraints on the relationship between seamount subduction, slow slip, and tremor at the north Hikurangi subduction zone, New Zealand. *Geophysical Research Letters*, *45*(23), 12–804. https://doi.org/10.1029/2018gl080259

Barker, D., Sutherland, R., Henrys, S., & Bannister, S. (2009). Geometry of the Hikurangi subduction thrust and upper plate, North Island, New Zealand. *Geochemistry, Geophysics, Geosystems*, *10*(2). https://doi.org/10.1029/2008gc002153

Barnes, P. M., Lamarche, G., Bialas, J., Henrys, S., Pecher, I., Netzeband, G. L., & Crutchley, G. (2010). Tectonic and geological framework for gas hydrates and cold seeps on the Hikurangi subduction margin, New Zealand. *Marine Geology*, *272*(1–4), 26–48. https://doi.org/10.1016/j.margeo.2009.03.012

Barnes, P. M., Nicol, A., & Harrison, T. (2002). Late Cenozoic evolution and earthquake potential of an active listric thrust complex above the Hikurangi subduction zone, New Zealand. *The Geological Society of America Bulletin*, *114*(11), 1379–1405. https://doi.org/10.1130/0016-7606(2002)114<1379:lceaep>2.0.co;2

Barnes, P. M., Wallace, L. M., Saffer, D. M., Bell, R. E., Underwood, M. B., Fagereng, A., et al. (2020). Slow slip source characterized by lithological and geometric heterogeneity. *Science Advances*, *6*(13), eaay3314. https://doi.org/10.1126/sciadv.aay3314

Beanland, S., & Haines, J. (1998). The kinematics of active deformation in the North Island, New Zealand, determined from geological strain rates. *New Zealand Journal of Geology and Geophysics*, *41*(4), 311–323. https://doi.org/10.1080/00288306.1998.9514813

Becker, J., Sandwell, D., Smith, W., Braud, J., Binder, B., Depner, J., et al. (2009). Global bathymetry and elevation data at 30 arc seconds resolution: SRTM30_PLUS. *Marine Geodesy*, *32*(4), 355–371. https://doi.org/10.1080/01490410903297766

Bell, R., Holden, C., Power, W., Wang, X., & Downes, G. (2014). Hikurangi margin tsunami earthquake generated by slow seismic rupture over a subducted seamount. *Earth and Planetary Science Letters*, *397*, 1–9. https://doi.org/10.1016/j.epsl.2014.04.005

Bell, R., Sutherland, R., Barker, D., Henrys, S., Bannister, S., Wallace, L., & Beavan, J. (2010). Seismic reflection character of the Hikurangi subduction interface, New Zealand, in the region of repeated Gisborne slow slip events. *Geophysical Journal International*, *180*(1), 34–48. https://doi.org/10.1111/j.1365-246x.2009.04401.x

Bozdağ, E., Peter, D., Lefebvre, M., Komatitsch, D., Tromp, J., Hill, J., & Pugmire, D. (2016). Global adjoint tomography: First-generation model. *Geophysical Journal International*, *207*(3), 1739–1766.

Byrne, D. E., Wang, W.-h., & Davis, D. M. (1993). Mechanical role of backstops in the growth of forearcs. *Tectonics*, *12*(1), 123–144. https://doi.org/10.1029/92tc00618

Carter, R. M., & Naish, T. R. (1998). A review of Wanganui Basin, New Zealand: Global reference section for shallow marine, Plio–Pleistocene (2.5–0 Ma) cyclostratigraphy. *Sedimentary Geology*, *122*(1–4), 37–52. https://doi.org/10.1016/s0037-0738(98)00097-9

Chesley, C., Naif, S., Key, K., & Bassett, D. (2021). Fluid-rich subducting topography generates anomalous forearc porosity. *Nature*, *595*(7866), 255–260. https://doi.org/10.1038/s41586-021-03619-8

Chow, B., Kaneko, Y., Tape, C., Modrak, R., Mortimer, N., Bannister, S., & Townend, J. (2022). Strong upper-plate heterogeneity at the Hikurangi subduction margin (North Island, New Zealand) imaged by adjoint tomography. *Journal of Geophysical Research: Solid Earth*, *127*, e2021JB022865.

Chow, B., Kaneko, Y., Tape, C., Modrak, R., & Townend, J. (2020). An automated workflow for adjoint tomography—Waveform misfits and synthetic inversions for the North Island, New Zealand. *Geophysical Journal International*, *223*(3), 1461–1480. https://doi.org/10.1093/gji/ggaa381

Christensen, N. I. (1996). Poisson's ratio and crustal seismology. *Journal of Geophysical Research: Solid Earth*, *101*(B2), 3139–3156. https://doi.org/10.1029/95jb03446

Cloos, M., & Shreve, R. L. (1996). Shear-zone thickness and the seismicity of Chilean- and Marianas-type subduction zones. *Geology*, *24*(2), 107. https://doi.org/10.1130/0091-7613(1996)024<0107:sztats>2.3.co;2

Collot, J.-Y., Delteil, J., Lewis, K. B., Davy, B., Lamarche, G., Audru, J.-C., et al. (1996). From oblique subduction to intra-continental transpression: Structures of the southern Kermadec-Hikurangi margin from multibeam bathymetry, side-scan sonar and seismic reflection. *Marine Geophysical Researches*, *18*(2), 357–381. https://doi.org/10.1007/bf00286085

Cummins, P. R., Baba, T., Kodaira, S., & Kaneda, Y. (2002). The 1946 Nankai earthquake and segmentation of the Nankai Trough. *Physics of the Earth and Planetary Interiors*, *132*(1–3), 75–87. https://doi.org/10.1016/s0031-9201(02)00045-6

Delahaye, E., Townend, J., Reyners, M., & Rogers, G. (2009). Microseismicity but no tremor accompanying slow slip in the Hikurangi subduction zone, New Zealand. *Earth and Planetary Science Letters*, *277*(1–2), 21–28. https://doi.org/10.1016/j.epsl.2008.09.038

Dominguez, S., Lallemand, S., Malavieille, J., & von Huene, R. (1998). Upper plate deformation associated with seamount subduction. *Tectonophysics*, *293*(3–4), 207–224. https://doi.org/10.1016/s0040-1951(98)00086-9

Dominguez, S., Malavieille, J., & Lallemand, S. E. (2000). Deformation of accretionary wedges in response to seamount subduction: Insights from sandbox experiments. *Tectonics*, *19*(1), 182–196. https://doi.org/10.1029/1999tc900055

Eberhart-Phillips, D., & Bannister, S. (2015). 3-D imaging of the northern Hikurangi subduction zone, New Zealand: Variations in subducted sediment, slab fluids and slow slip. *Geophysical Journal International*, *201*(2), 838–855. https://doi.org/10.1093/gji/ggv057

Eberhart-Phillips, D., Bannister, S., Reyners, M., & Henrys, S. (2020). New Zealand Wide model 2.2 seismic velocity and Qs and Qp models for New Zealand [dataset]. Zenodo. https://doi.org/10.5281/zenodo.3779523

Eberhart-Phillips, D., Han, D.-H., & Zoback, M. D. (1989). Empirical relationships among seismic velocity, effective pressure, porosity, and clay content in sandstone. *Geophysics*, *54*(1), 82–89.

Eberhart-Phillips, D., Reyners, M., & Bannister, S. (2015). A 3D QP attenuation model for all of New Zealand. *Seismological Research Letters*, *86*(6), 1655–1663. https://doi.org/10.1785/0220150124

Eberhart-Phillips, D., Reyners, M., Chadwick, M., & Chiu, J.-M. (2005). Crustal heterogeneity and subduction processes: 3-D Vp, Vp/Vs and Q in the southern North Island, New Zealand. *Geophysical Journal International*, *162*(1), 270–288. https://doi.org/10.1111/j.1365-246x.2005.02530.x

Edbrooke, S., Heron, D., Forsyth, P., & Jongens, R. (2015). *Geological Map of New Zealand 1:1,000,000* (Vol. 2). GNS Science Geological Map.

Ellis, S., Fagereng, A., Barker, D., Henrys, S., Saffer, D., Wallace, L., et al. (2015). Fluid budgets along the northern Hikurangi subduction margin, New Zealand: The effect of a subducting seamount on fluid pressure. *Geophysical Journal International*, *202*(1), 277–297. https://doi.org/10.1093/gji/ggv127

Fichtner, A., Bunge, H.-P., & Igel, H. (2006a). The adjoint method in seismology: I. Theory. *Physics of the Earth and Planetary Interiors*, *157*(1–2), 86–104. https://doi.org/10.1016/j.pepi.2006.03.016

Fichtner, A., Bunge, H.-P., & Igel, H. (2006b). The adjoint method in seismology—: II. Applications: Traveltimes and sensitivity functionals. *Physics of the Earth and Planetary Interiors*, *157*(1–2), 105–123. https://doi.org/10.1016/j.pepi.2006.03.018

Fichtner, A., & Trampert, J. (2011). Resolution analysis in full waveform inversion. *Geophysical Journal International*, *187*(3), 1604–1624. https://doi.org/10.1111/j.1365-246x.2011.05218.x

Frederik, M. C., Gulick, S. P., & Miller, J. J. (2020). Effect on subduction of deeply buried seamounts offshore of Kodiak Island. *Tectonics*, *39*(7), e2019TC005710. https://doi.org/10.1029/2019tc005710

Heise, W., Caldwell, T. G., Bannister, S., Bertrand, E., Ogawa, Y., Bennie, S., & Ichihara, H. (2017). Mapping subduction interface coupling using magnetotellurics: Hikurangi margin, New Zealand. *Geophysical Research Letters*, *44*(18), 9261–9266. https://doi.org/10.1002/2017gl074641

Hunt, T., & Glover, R. (1995). *Origin of mineral springs on the east coast, North Island, NZ*. (Tech. Rep.). Wairakei Research Centre, IGNS.

Ito, H., DeVilbiss, J., & Nur, A. (1979). Compressional and shear waves in saturated rock during water-steam transition. *Journal of Geophysical Research: Solid Earth*, *84*(B9), 4731–4735. https://doi.org/10.1029/jb084ib09p04731

Jacobs, K., Savage, M., & Smith, E. (2016). Quantifying seismicity associated with slow slip events in the Hikurangi margin, New Zealand. *New Zealand Journal of Geology and Geophysics*, *59*(1), 58–69. https://doi.org/10.1080/00288306.2015.1127827

Kanamori, H. (1972). Mechanism of tsunami earthquakes. *Physics of the Earth and Planetary Interiors*, *6*(5), 346–359. https://doi.org/10.1016/0031-9201(72)90058-1

King, P. R., & Thrasher, G. P. (1996). *Cretaceous-Cenozoic Geology and Petroleum Systems of the Taranaki Basin, New Zealand* (Vol. 2). Institute of Geological & Nuclear Sciences.

Kobe, H. W., & Pettinga, J. R. (1984). Red Island (NZ) and its submarine-exhalative Mn-Fe mineralization. *Syngenesis and Epigenesis in the Formation of Mineral Deposits*, 562–572.

Kodaira, S., Takahashi, N., Nakanishi, A., Miura, S., & Kaneda, Y. (2000). Subducted seamount imaged in the rupture zone of the 1946 Nankaido earthquake. *Science*, *289*(5476), 104–106. https://doi.org/10.1126/science.289.5476.104

Komatitsch, D., & Tromp, J. (2002a). Spectral-element simulations of global seismic wave propagation—II. Three-dimensional models, oceans, rotation and self-gravitation. *Geophysical Journal International*, *150*(1), 303–318. https://doi.org/10.1046/j.1365-246x.2002.01716.x

Komatitsch, D., & Tromp, J. (2002b). Spectral-element simulations of global seismic wave propagation—I. Validation. *Geophysical Journal International*, *149*(2), 390–412. https://doi.org/10.1046/j.1365-246x.2002.01653.x

Lewis, K., & Pettinga, J. (1993). The emerging, imbricate frontal wedge of the Hikurangi margin. *Sedimentary Basins of the World*, *2*, 225–250.

Lewis, K. B., Carter, L., & Davey, F. J. (1994). The opening of Cook Strait: Interglacial tidal scour and aligning basins at a subduction to transform plate edge. *Marine Geology*, *116*(3–4), 293–312. https://doi.org/10.1016/0025-3227(94)90047-7

Lewis, K. B., Collot, J.-Y., & Lallem, S. E. (1998). The dammed Hikurangi trough: A channel-fed trench blocked by subducting seamounts and their wake avalanches (New Zealand–France GeodyNZ Project). *Basin Research*, *10*(4), 441–468. https://doi.org/10.1046/j.1365-2117.1998.00080.x

Litchfield, N., Ellis, S., Berryman, K., & Nicol, A. (2007). Insights into subduction-related uplift along the Hikurangi Margin, New Zealand, using numerical modeling. *Journal of Geophysical Research: Earth Surface*, *112*(F2). https://doi.org/10.1029/2006jf000535

Litchfield, N., Van Dissen, R., Sutherland, R., Barnes, P., Cox, S., Norris, R., et al. (2014). A model of active faulting in New Zealand. *New Zealand Journal of Geology and Geophysics*, *57*(1), 32–56. https://doi.org/10.1080/00288306.2013.854256

Marcaillou, B., Collot, J.-Y., Ribodetti, A., d'Acremont, E., Mahamat, A.-A., & Alvarado, A. (2016). Seamount subduction at the North-Ecuadorian convergent margin: Effects on structures, inter-seismic coupling and seismogenesis. *Earth and Planetary Science Letters*, *433*, 146–158. https://doi.org/10.1016/j.epsl.2015.10.043

Martinez-Loriente, S., Sallarès, V., Ranero, C. R., Ruh, B. J., Barckhausen, U., Grevemeyer, I., & Bangs, N. (2019). Influence of incoming plate relief on overriding plate deformation and earthquake Nucleation: Cocos Ridge Subduction (Costa Rica). *Tectonics*, *38*(12), 4360–4377.

Mitchell, J. S., Mackay, K. A., Neil, H. L., Mackay, E. J., Pallentin, A., & Notman, P. (2012). *Undersea New Zealand, 1:5,000,000*. Retrieved from https://niwa.co.nz/our-science/oceans/bathymetry/download-the-data

Mortimer, N. (2004). New Zealand's geological foundations. *Gondwana Research*, *7*(1), 261–272. https://doi.org/10.1016/s1342-937x(05)70324-5

Naif, S., Key, K., Constable, S., & Evans, R. L. (2015). Water-rich bending faults at the Middle America Trench. *Geochemistry, Geophysics, Geosystems*, *16*(8), 2582–2597. https://doi.org/10.1002/2015gc005927

Nicol, A., Mazengarb, C., Chanier, F., Rait, G., Uruski, C., & Wallace, L. (2007). Tectonic evolution of the active Hikurangi subduction margin, New Zealand, since the Oligocene. *Tectonics*, *26*(4). https://doi.org/10.1029/2006tc002090

Nocedal, J., & Wright, S. (2006). *Numerical optimization*. Springer Science & Business Media.

Pedley, K. L., Barnes, P. M., Pettinga, J. R., & Lewis, K. B. (2010). Seafloor structural geomorphic evolution of the accretionary frontal wedge in response to seamount subduction, Poverty Indentation, New Zealand. *Marine Geology*, *270*(1–4), 119–138. https://doi.org/10.1016/j.margeo.2009.11.006

Pettinga, J. R. (1982). Upper Cenozoic structural history, coastal Southern Hawke's Bay, New Zealand. *New Zealand Journal of Geology and Geophysics*, *25*(2), 149–191. https://doi.org/10.1080/00288306.1982.10421407

Pita Sllim, O. (2021). *Spatiotemporal analysis of repeating earthquakes near Porangahau, Hikurangi Margin, New Zealand*. (Unpublished master's thesis). Open Access Victoria University of Wellington– Te Herenga Waka.

Prendergast, E., & Offler, R. (2012). Underplated seamount in the Narooma accretionary complex, NSW, Australia. *Lithos*, *154*, 224–234. https://doi.org/10.1016/j.lithos.2012.07.010

Ranero, C. R., Morgan, J. P., McIntosh, K., & Reichert, C. (2003). Bending-related faulting and mantle serpentinization at the Middle America trench. *Nature*, *425*(6956), 367–373. https://doi.org/10.1038/nature01961

Reyes, A., Christenson, B., & Faure, K. (2010). Sources of solutes and heat in low-enthalpy mineral waters and their relation to tectonic setting, New Zealand. *Journal of Volcanology and Geothermal Research*, *192*(3–4), 117–141. https://doi.org/10.1016/j.jvolgeores.2010.02.015

Reyners, M., Eberhart-Phillips, D., & Bannister, S. (2017). Subducting an old subduction zone sideways provides insights into what controls plate coupling. *Earth and Planetary Science Letters*, *466*, 53–61. https://doi.org/10.1016/j.epsl.2017.03.004

Ristau, J. (2008). Implementation of routine regional moment tensor analysis in New Zealand. *Seismological Research Letters*, *79*(3), 400–415. https://doi.org/10.1785/gssrl.79.3.400

Ristau, J. (2013). Update of regional moment tensor analysis for earthquakes in New Zealand and adjacent offshore regions. *Bulletin of the Seismological Society of America*, *103*(4), 2520–2533. https://doi.org/10.1785/0120120339

Ruh, J. B., Sallarès, V., Ranero, C. R., & Gerya, T. (2016). Crustal deformation dynamics and stress evolution during seamount subduction: High-resolution 3-D numerical modeling. *Journal of Geophysical Research: Solid Earth*, *121*(9), 6880–6902. https://doi.org/10.1002/2016jb013250

Scholz, C. H., & Small, C. (1997). The effect of seamount subduction on seismic coupling. *Geology*, *25*(6), 487–490. https://doi.org/10.1130/0091-7613(1997)025<0487:teosso>2.3.co;2

Singh, S. C., Hananto, N., Mukti, M., Robinson, D. P., Das, S., Chauhan, A., et al. (2011). Aseismic zone and earthquake segmentation associated with a deep subducted seamount in Sumatra. *Nature Geoscience*, *4*(5), 308–311. https://doi.org/10.1038/ngeo1119

Sun, T., Saffer, D., & Ellis, S. (2020). Mechanical and hydrological effects of seamount subduction on megathrust stress and slip. *Nature Geoscience*, *13*(3), 249–255. https://doi.org/10.1038/s41561-020-0542-0

Tao, K., Grand, S. P., & Niu, F. (2018). Seismic structure of the upper mantle beneath eastern Asia from full waveform seismic tomography. *Geochemistry, Geophysics, Geosystems*, *19*(8), 2732–2763. https://doi.org/10.1029/2018gc007460

Tape, C., Liu, Q., & Tromp, J. (2007). Finite-frequency tomography using adjoint methods—Methodology and examples using membrane surface waves. *Geophysical Journal International*, *168*(3), 1105–1129. https://doi.org/10.1111/j.1365-246x.2006.03191.x

Tarantola, A. (1984). Inversion of seismic reflection data in the acoustic approximation. *Geophysics*, *49*(8), 1259–1266. https://doi.org/10.1190/1.1441754

Tromp, J., Tape, C., & Liu, Q. (2005). Seismic tomography, adjoint methods, time reversal and banana-doughnut kernels. *Geophysical Journal International*, *160*(1), 195–216.

Von Huene, R., & Scholl, D. W. (1991). Observations at convergent margins concerning sediment subduction, subduction erosion, and the growth of continental crust. *Reviews of Geophysics*, *29*(3), 279–316. https://doi.org/10.1029/91rg00969

Wallace, L. (2020). Slow slip events in New Zealand. *Annual Review of Earth and Planetary Sciences*, *48*, 175–203. https://doi.org/10.1146/annurev-earth-071719-055104

Wallace, L., Barnes, P., Beavan, J., Van Dissen, R., Litchfield, N., Mountjoy, J., & Pondard, N. (2012). The kinematics of a transition from subduction to strike-slip: An example from the central New Zealand plate boundary. *Journal of Geophysical Research: Solid Earth*, *117*(B2). https://doi.org/10.1029/2011jb008640

Wallace, L., Beavan, J., Bannister, S., & Williams, C. (2012). Simultaneous long-term and short-term slow slip events at the Hikurangi subduction margin, New Zealand: Implications for processes that control slow slip event occurrence, duration, and migration. *Journal of Geophysical Research: Solid Earth*, *117*(B11). https://doi.org/10.1029/2012jb009489

Wallace, L., Beavan, J., McCaffrey, R., & Darby, D. (2004). Subduction zone coupling and tectonic block rotations in the North Island, New Zealand. *Journal of Geophysical Research: Solid Earth*, *109*(B12). https://doi.org/10.1029/2004jb003241

Wallace, L., Reyners, M., Cochran, U., Bannister, S., Barnes, P., Berryman, K., et al. (2009). Characterizing the seismogenic zone of a major plate boundary subduction thrust: Hikurangi Margin, New Zealand. *Geochemistry, Geophysics, Geosystems*, *10*(10). https://doi.org/10.1029/2009GC002610

Wang, K., & Bilek, S. L. (2011). Do subducting seamounts generate or stop large earthquakes? *Geology*, *39*(9), 819–822. https://doi.org/10.1130/g31856.1

Warren-Smith, E., Fry, B., Wallace, L., Chon, E., Henrys, S., Sheehan, A., et al. (2019). Episodic stress and fluid pressure cycling in subducting oceanic crust during slow slip. *Nature Geoscience*, *12*(6), 475–481. https://doi.org/10.1038/s41561-019-0367-x

Williams, C., Eberhart-Phillips, D., Bannister, S., Barker, D., Henrys, S., Reyners, M., & Sutherland, R. (2013). Revised interface geometry for the Hikurangi subduction zone, New Zealand. *Seismological Research Letters*, *84*(6), 1066–1073. https://doi.org/10.1785/0220130035

Wilson, C., Gravley, D., Leonard, G., & Rowland, J. (2009). Volcanism in the central Taupo volcanic zone, New Zealand: Tempo, styles and controls. *Studies in Volcanology: The Legacy of George Walker*. Special Publications of IAVCEI, 2, 225–247.

Wilson, C., Houghton, B., McWilliams, M., Lanphere, M., Weaver, S., & Briggs, R. (1995). Volcanic and structural evolution of Taupo Volcanic Zone, New Zealand: A review. *Journal of Volcanology and Geothermal Research*, *68*(1–3), 1–28. https://doi.org/10.1016/0377-0273(95)00006-g

Yang, H., Liu, Y., & Lin, J. (2013). Geometrical effects of a subducted seamount on stopping megathrust ruptures. *Geophysical Research Letters*, *40*(10), 2011–2016. https://doi.org/10.1002/grl.50509

Zal, H. J., Jacobs, K., Savage, M. K., Yarce, J., Mroczek, S., Graham, K., et al. (2020). Temporal and spatial variations in seismic anisotropy and Vp/Vs ratios in a region of slow slip. *Earth and Planetary Science Letters*, *532*, 115970. https://doi.org/10.1016/j.epsl.2019.115970

Zhu, H., Bozdağ, E., & Tromp, J. (2015). Seismic structure of the European upper mantle based on adjoint tomography. *Geophysical Journal International*, *201*(1), 18–52. https://doi.org/10.1093/gji/ggu492